Cell-free DNA whole-genomes reveal chromosomal rearrangements associated with heterogeneity and stem cell-like castration-resistant prostate cancer

Authors: Marjorie L. Roskes[1,2,3,4*], Alexander Martinez-Fundichely[1,2,3,4*], Sandra Cohen[1], Metin Balaban[5], Chen Khuan Wong[6], Weiling Li[1,2,3,4], Tonatiuh A. Gonzalez[1,2,3,4], Anisha B. Tehim[7], Hao Xu[8], Shahd ElNaggar[9], Matthew Myers[5], Rohan Bareja[4], Princesca Dorsaint[4], Kathryn Gorski[4], Muhammad Asad[10], Majd Al Assaad[4,10], Brian D. Robinson[1,4,10], Michael Sigouros[4], Ethan Barnett[11], Jyothi Manohar[4], Scott Tagawa[1,4,12], David Nanus[1,4,12], Ana Molina[1,4,12], Jones T. Nauseef[1,4,12], Cora N. Sternberg[1,4,12], Juan Miguel Mosquera[1,4,10], Howard I. Scher[11], Andrea Sboner[1,4], Benjamin J. Raphael[5], Yu Chen[6,11,12,#], Ekta Khurana[1,2,3,4,#]

[1]Sandra and Edward Meyer Cancer Center, Weill Cornell Medicine, New York, NY 10021, USA
[2]Institute for Computational Biomedicine, Weill Cornell Medicine, New York, NY 10021, USA
[3]Department of Physiology and Biophysics, Weill Cornell Medicine, New York, NY 10021, USA
[4]Englander Institute for Precision Medicine, Weill Cornell Medicine, New York, NY 10021, USA
[5]Department of Computer Science, Princeton University, New Jersey, USA
[6]Human Oncology and Pathogenesis Program, Department of Medicine, Memorial Sloan Kettering Cancer Center, New York, NY 10065, USA
[7]Department of Biological Statistics and Computational Biology, Cornell University, Ithaca, NY 14850, USA
[8]School of Computer Science, McGill University, Montreal, QC, H3A 0G4, Canada
[9]Department of Biology, Barnard College, Columbia University, New York, NY 10027, USA
[10]Department of Pathology and Laboratory Medicine, Weill Cornell Medicine, New York, NY 10065, USA
[11]Department of Medicine, Memorial Sloan Kettering Cancer Center, New York, NY 10065, USA
[12]Department of Medicine, Weill Cornell Medicine and New York–Presbyterian Hospital, New York, NY 10065, USA

[*]These authors contributed equally to this work.
[#]Corresponding author. Email: cheny1@mskcc.org; ekk2003@med.cornell.edu

The authors declare no potential conflicts of interest.

Abstract

Castration-resistant prostate cancer (CRPC) is an aggressive disease exhibiting multiple epigenomic subtypes: androgen receptor-dependent CRPC-AR, and lineage plastic subtypes CRPC-SCL (stem cell-like), CRPC-WNT (Wnt-dependent), and CRPC-NE (neuroendocrine). By transcriptomic profiling of tissue, and whole-genome sequencing (WGS) of tissue and cell-free DNA (cfDNA) from 500 samples, we relate genomic variants with epigenomic state. We find lineage plasticity is associated with higher epigenomic and genomic heterogeneity. Samples with CRPC-SCL show higher chromosomal instability. We find DNA alterations, particularly chromosomal rearrangements, in the YAP/TAZ pathway associated with CRPC-SCL. For example, complex rearrangements on chromosome 4, which are supported by patient-matched 3D genome architecture data, decrease promoter interactions of *MOB1B*, a YAP/TAZ pathway inhibitor, with its enhancers. Together, the genomic variants in the pathway can predict CRPC-SCL with 79% accuracy. We show the utility of cfDNA WGS for joint inference of epigenomic state and genomic variants, which can guide patient stratification for clinical decisions.

Significance

This study reveals genomic variants associated with the presence of lineage-plastic CRPC stem cell-like state. We leverage the utility of minimally invasive cfDNA sequencing to obtain genomic and epigenomic insights about CRPC heterogeneity, which have implications for patient stratification for treatment decisions.

Introduction

In the treatment-naïve stage, the growth of prostate cancer is largely dependent on the androgen receptor (AR) pathway. As such, the first line of treatment for advanced prostate cancer is androgen deprivation therapy (ADT). Tumors often develop resistance to ADT and are termed castration-resistant prostate cancer (CRPC). Thus, often next generation AR signaling inhibitors (ARSIs)[1–4] are used in combination with ADT as a first-line therapy. ARSIs work to inhibit AR signaling by different mechanisms. For example, abiraterone inhibits steroidogenesis of adrenal androgens, while enzalutamide and apalutamide inhibit translocation of the AR dimer to the nucleus thereby blocking DNA and cofactor binding[5]. Selective pressure can result in tumors that acquire resistance to ARSIs, either by way of genomic alterations of AR such as amplification of the AR gene or alternative splicing of AR mRNA, or by circumventing dependence on AR altogether[5]. While some of these lineage plastic, AR-independent tumors transdifferentiate into a state with neuroendocrine histology, others remain in the non-AR, non-neuroendocrine state, often referred to as “double-negative” prostate cancer, retaining their adenocarcinoma histology[6,7].

By using chromatin and transcriptomic profiling, we identified four subtypes of CRPC: CRPC-AR which depends on the AR pathway, CRPC-SCL which overexpresses stem cell-like markers, CRPC-WNT which is dependent on the WNT signaling pathway, and CRPC-NE which constitutes the neuroendocrine tumors expressing neuroendocrine gene markers[8]. CRPC-WNT and CRPC-SCL tumors also exhibit enrichment of fibroblast growth factor receptor (FGFR) signaling, consistent with previous studies of double-negative tumors[6]. Moreover, CRPC-SCL tumors also exhibit overexpression of Janus kinase/signal transducer and activator of transcription (JAK/STAT) signaling, which has been shown to drive lineage plasticity in CRPC[6,9]. Here, we refer to CRPC-SCL, CRPC-WNT, and CRPC-NE as lineage plastic subtypes since they show divergence from the CRPC-AR state.

The identification of these four subtypes in patient tumors is critical since it can offer therapeutic opportunities[8]. While recent efforts have found evidence of intra-patient CRPC subtype heterogeneity,

they were limited by small patient cohorts and did not examine the extent of heterogeneity in the context of all these four subtypes[10,11]. The CRPC-SCL subtype in particular has not been characterized well by previous studies. While genomic events have been associated with CRPC-AR (alterations of the AR gene and enhancer), CRPC-NE (loss of RB1), and CRPC-WNT (alterations in the Wnt signaling pathway), no such events have been described for CRPC-SCL[8,12–17].

In this study, we seek to fill these gaps via a combined analysis of genomic events and the four epigenomic subtypes, defined by their gene expression and chromatin accessibility profiles. To do so, we annotate the samples with epigenomic subtypes by quantifying the fractional contribution of each using tissue RNA-seq and/or nucleosomal profiling using cell-free DNA (cfDNA) whole-genome sequencing (WGS). We then relate the genomic events with the epigenomic subtypes by analyzing matched WGS and RNA-seq in the tissue cohort, as well as WGS in the cfDNA cohort.

We find novel genomic alterations at the YAP/TAZ pathway genes that are associated with CRPC-SCL. Because genomic alterations can be difficult to interpret in the absence of other data types, we used matched Hi-C, which reveals three-dimensional (3D) genome architecture, to validate their presence and infer their functional impact[18]. Additionally, we find associations of epigenomic subtypes with genomic instability and heterogeneity, as computed from copy number alterations (CNAs) and structural variations (SVs).

Results

Overview of patient samples used in the study

To perform a combined analysis of genomic events and epigenomic subtypes, we annotate the samples by quantifying the fractional contribution of each CRPC subtype. This is done by using deconvolution approaches on tissue RNA-seq (n=455) and nucleosome profiling from cfDNA WGS (n=68)[8,10,14,15,19,20] (fig. 1A, 2A,B). We then relate the genomic events from WGS with the epigenomic subtypes. This is done by using the patient samples for whom both RNA-seq and WGS was performed on tissue (n=105), as well as the cfDNA whole-genomes[14,21]. Since both genomic variants and epigenomic subtypes are inferred from the same WGS data, the cfDNA whole-genomes in particular offer a unique opportunity to examine their relationship at the same tumoral state and timepoint[15]. Moreover, the use of cfDNA whole-genomes offers the opportunity to monitor the progression of tumors into different epigenomic subtypes with the accompanying genomic changes. Additionally, since prostate cancer genomic alterations are dominated by large SVs[22–25], the use of deep WGS is important to capture the whole spectrum of genomic events as they may relate to chromatin-based subtypes. Due to the limited availability of deep cfDNA WGS of lineage plastic subtypes (n=2 among n=35 patients[15]), we sequenced additional patient samples (n=20) at 40X coverage from Weill Cornell Medicine (WCM) and Memorial Sloan Kettering (MSK) (fig. 1B). For 7 of these 20 samples, we also had RNA-seq from tissue obtained at the same timepoint as plasma, allowing comparison of molecular subtypes inferred from tissue RNA-seq versus cfDNA WGS. cfDNA whole-genomes from an additional control cohort of healthy participants (n=14) were sequenced to account for the signal from peripheral blood mononuclear cells (PBMCs) in estimating tumoral subtypes from cfDNA (table S1).

Inter- and intra- Sample CRPC subtype heterogeneity in different histological classes

Due to the concordance of the four molecular subtypes identified from chromatin (ATAC-seq) and transcriptomic (RNA-seq) profiling[8], we used their signature genes and accessible chromatin sites to infer their presence in patient samples from RNA-seq and cfDNA WGS, respectively. Signature expression genes for each subtype were defined as those showing subtype-specific expression in cell lines/organoids[8] (tables S2, S3). By comparing expression profiles of subtype-specific signature genes

137 in patient samples to that in cell lines/organoids, we can estimate the fractional contribution of each
138 CRPC subtype (fig. 2A, S1A, S2A) (table S4)[20]. For cfDNA, we leverage the fact that it is enriched for
139 nucleosome-bound regions in tumor tissue[26]. The aggregate coverage profile across cfDNA samples
140 from patient-derived xenografts (PDXs) was computed for subtype-specific accessible chromatin sites.
141 To account for the signal from PBMCs inherent in cfDNA, we generated a panel of no-cancer controls
142 (n=14) (table S5). By comparing coverage profiles in subtype-specific signature sites in patient samples
143 to that of the PDX-derived signature, we can estimate the fractional contribution of each CRPC subtype
144 (fig. 2B, S1B) (tables S6, S7)[10]. The strength of these deconvolution approaches is that they allow
145 assignment of a single sample to a mixture of multiple subtypes.
146
147 To validate the assignment of samples to different subtypes, we checked the expression of the top,
148 well-studied subtype-specific marker genes and pathways (table S8)[8]. As expected, we find that *AR* is
149 upregulated in CRPC-AR samples[27] (fig. S3A). Interestingly, we find that *TP53* and *PTEN* are
150 downregulated in lineage plastic samples, the mutational loss of which has been reported to be
151 associated with lineage plasticity and aggressive disease in CRPC[8,17,28] (fig. S3B). Similarly, *RB1* is
152 downregulated while *ASCL1*, *NEUROD1*, *SYP*, and genes in the NEPC pathway are upregulated in
153 CRPC-NE[8,29] (fig S3C). CRPC-WNT samples show overexpression of genes in the WNT pathway[27]
154 (fig. S3D), while CRPC-SCL samples show upregulation of many of the YAP/TAZ pathway target genes
155 (fig. S3E)[8]. Furthermore, we find that CRPC-SCL patients show shorter survival on ARSIs than those
156 without CRPC-SCL, consistent with their dependence on transcription factors (TFs) other than AR (fig.
157 2C)[8]. Furthermore, to confirm that non-tumor cells do not influence the CRPC subtype fraction
158 estimation, we used single-cell RNA-seq (scRNA-seq) data from CRPC patients that allows annotation
159 of each cell as tumoral or non-tumoral[30]. To compare with our approach, we created pseudo-bulk RNA-
160 seq from only tumor cells and all cells. We then computed the fractional components estimated in
161 pseudo-bulk from all cells versus that from tumor cells only and find high concordance, even in samples
162 with tumor fraction as low as 0.13 (fig. 3A, B). This shows that the signature genes and the
163 deconvolution approach used in our study allows accurate assessment of the subtypes from bulk RNA-
164 seq.
165
166 Although samples are generally classified as adenocarcinoma, neuroendocrine, or mixed based on
167 histology clinically, we find that molecularly they are, in fact, quite heterogeneous[31]. While most of the
168 adenocarcinoma samples (96% for tissue and 94% for cfDNA) showed evidence of CRPC-AR as
169 expected, a large majority show some fraction of other molecular subtypes (76% for tissue and 60%
170 for cfDNA). These include 33% with CRPC-SCL, 28% with CRPC-WNT, and 28% with CRPC-NE (fig.
171 S2B, C). Similarly, while most neuroendocrine samples show evidence of CRPC-NE (89% for tissue
172 and 70% for cfDNA), many of them also show presence of other subtypes. CRPC-SCL is the most
173 common molecular subtype in adenocarcinoma samples after CRPC-AR, and CRPC-WNT is the most
174 common subtype in neuroendocrine samples after CRPC-NE (fig. S2B, C).
175
176 We find that the samples with the presence of any of the lineage plastic subtypes tend to be more
177 heterogeneous: these samples most often have co-occurrence of multiple CRPC subtypes. This
178 phenomenon is especially true for the CRPC-SCL subtype, which co-occurs with other subtypes in 99%
179 of cases (fig. 3C, D). We compared the ratio of numbers of samples with mixed subtypes to single
180 subtype and call this the subtype mixture index. We find that CRPC-SCL, CRPC-WNT, and CRPC-NE
181 have significantly higher mixture index values than CRPC-AR samples, which exhibit single subtype in
182 33% of the cases (fig. 3E). Although CRPC-NE has significantly higher subtype mixture index than
183 CRPC-AR, we find that the samples contributing to the higher index are from the adenocarcinoma
184 histology. In other words, when CRPC-NE exists as the only subtype at the molecular level, it has
185 neuroendocrine histology, while its existence in adenocarcinoma samples is in the presence of other
186 subtypes, mostly CRPC-AR (Fisher's Exact Odds Ratio = 18.85, P = 1.21e-10) (fig. S2D). This trend is

as expected and shows that histology-based classification may miss the beginning of lineage plasticity, which is captured by our molecular annotation. Thus, molecular annotations, when used together with histological classifications, can have clinical relevance by capturing the transition to lineage plasticity, and beginning of treatment resistance.

Enrichment of subtypes at different metastatic sites

Formation of metastases at distant sites is a key feature of cancer and cancer-related death[32]. In order for a metastasis to form, a tumor cell has to invade the blood stream, survive intense combat with the immune system, exit the bloodstream, and colonize at a distant site[33]. Different tumor cells are more prone to seeding in specific distant sites, a phenomenon known as organ tropism, which is largely influenced by the compatibility of the site-specific microenvironment to the tumor cell[33]. Moreover, the tendencies of tumor cells to metastasize to specific sites can be subtype-specific within a given cancer type[34]. While bone is the most common site of prostate cancer metastasis, other sites are also frequently found. In light of this, we next looked for metastatic site enrichment in tissue RNA-seq data across CRPC subtypes to determine if specific CRPC subtypes are more likely to originate from a particular site. To avoid double counting, the samples were annotated as belonging to a subtype if they showed it as their major subtype (>50%). Consistent with previous studies, we find that CRPC-NE samples are more likely to be from liver (Fisher's Exact Odds Ratio = 5.45, P = 6e-6, fig. 4) and soft tissue (Fisher's Exact Odds Ratio = 3.55, P = 7.12e-3, fig. 4)[35,36]. While most samples from all sites are CRPC-AR (fig. S4), as expected, we do find enrichment of this subtype at lymph node (Fisher's Exact Odds Ratio = 3.37, P = 4.97e-7, fig. 4), which is consistent with previous reports[37].

We find that CRPC-SCL samples are more likely to originate from bone compared to other tissues (Fisher's Exact Odds Ratio = 6.03, P = 2e-6, fig. 4). This is consistent with previous reports that PC3 (a CRPC-SCL cell line) colonizes to bone in mice[38], and evidence of tumor cells with AP-1 signaling (that is characteristic of CRPC-SCL) in scRNA-seq from bone metastases[39]. A mechanistic study to examine how this occurs, found that protein regulator of cytokinesis 1 (PRC1), which has been implicated in promoting stemness in cancer, is elevated in prostate cancer cells with stem cell traits and drives colonization to the bone[38]. Moreover, it is well known that bone provides a unique niche for stem cells, in part because of its hypoxic microenvironment that promotes commitment to stemness[40]. Thus, we hypothesize that it is the bone microenvironment that makes it especially hospitable to CRPC-SCL, which is characterized by stem cell-like features.

Genomic alterations of the YAP/TAZ pathway associated with epigenomic subtypes

We identified genome-wide copy number alterations (CNAs), structural variants (SVs), and single nucleotide variants (SNVs) from WGS data from cfDNA and tissue. When matched WGS from cfDNA and tissue was available, we observe a high concordance of both type and breakpoints (for SVs) between called variants, showing the reliability of calling genomic alterations from cfDNA (fig. S5). Moreover, we observe multiple events that are consistent with previous studies. Samples with CRPC-AR are enriched for amplifications of the *AR* gene (fold change = 2; binomial p value = 2.55e-5; fig. 5B, S6B); those with CRPC-NE are enriched for biallelic inactivation of *RB1*[13,17,28] (fold change = 5.21; binomial p value = 1.41e-02, fig. S6C); and *CTNNB1* (β-catenin) mutations are enriched in CRPC-WNT samples (6.5% for CRPC-WNT vs. zero for others; binomial p value = 0; fig. S6D) (tables S9, S10, S11, S12, S13).

The chromatin accessibility landscape of CRPC-SCL has been shown to be enriched for binding sites of the AP-1 and TEAD families of TFs, which work together to promote the oncogenic growth of CRPC-SCL tumors[8]. Activation of the TEAD family is dependent on the YAP/TAZ pathway (fig. 5A). At baseline, the YAP/TAZ pathway is turned off by proteins such as TAOK1/2/3, NF2, WWC1, FRMD6,

235 SAV1, STK3/4, MOB1A/B, and LATS1/2 which work to phosphorylate, and thereby deactivate YAP1
236 and TAZ (an alias for WWTR1). In the absence of this deactivation mechanism, YAP1 and TAZ are in
237 their active form, and translocate to the nucleus to bind to and activate TEAD, which in turn likely works
238 with AP-1 to regulate the transition to CRPC-SCL[8,41]. Furthermore, YAP/TAZ target genes are
239 upregulated in the context of CRPC-SCL[8] (fig. S3E).
240
241 So far there have been no reports of CRPC-SCL-specific genomic alterations. YAP/TAZ pathway
242 alterations have been reported in many other cancers, and are most prevalent in mesothelioma, kidney
243 renal papillary cell carcinoma, and cervical squamous cell carcinoma[41]. In light of this, we sought to
244 leverage our unique dataset to describe the genomic alterations observed in CRPC. Indeed, we find
245 alterations of certain YAP/TAZ pathway genes enriched in samples with CRPC-SCL (fig. 5B, 5C).
246 These include complex rearrangements of chromosome 4 spanning the YAP/TAZ pathway inhibitor
247 *MOB1B* (fold change = 5.89, binomial p value = 1.10e-05, figs. 4B,C, S6E), and stopgain mutations in
248 another inhibitor, *LATS1* (7.4% for CRPC-SCL vs. zero for others, binomial p value = 0, figs. 5B,C). As
249 opposed to pathway inhibitors, we might expect activators to not be disabled in CRPC-SCL samples,
250 and indeed we observe a depletion of a complex rearrangement of chromosome 3 spanning the
251 YAP/TAZ pathway activator *TAZ* in these samples (fold change = 2.55, binomial p value = 4.60e-02,
252 fig. 5B,C, S6E). In our analysis, complex rearrangements are a type of SVs defined as large events
253 that span the entire gene or multiple genes. They are predicted to be either end-to-end telomere
254 translocations or pericentric inversions of the region and are supported by discordant reads at the
255 breakpoints upon manual inspection[41] (fig. S7). We hypothesize that these events may have functional
256 implications in regulating the genes, and thereby, the YAP/TAZ pathway.
257
258 A major advantage of using cfDNA is that it can be used for serial monitoring made feasible by its
259 simple and minimally invasive manner of collection. Similar to the previous observation of emergence
260 of biallelic inactivation of *RB1* accompanying the emergence of CRPC-NE in a patient (AE-180, fig.
261 5B)[15], we are able to track the co-evolution of *YAP/TAZ* pathway alterations with CRPC subtype using
262 cfDNA. The sample AE-129 began with presence of CRPC-SCL but showed reduction of this subtype
263 at progression on ARSIs accompanied with a complex rearrangement at chromosome 3 spanning the
264 *TAZ* gene, potentially inactivating the YAP/TAZ pathway (fig. 5B,D). Since most prostate tumors begin
265 as AR dependent, this example where we see reduction of CRPC-SCL and increase of CRPC-AR
266 potentially also points to the highly dynamic nature of lineage plasticity where patients may shift back
267 and forth between subtypes and highlights the power of using cfDNA to detect such transitions.
268

269 **Hi-C data validates complex rearrangements and shows they reduce access of *MOB1B and TAZ***
270 **to their cis-regulatory elements**

271 Large-scale chromosomal alterations have been implicated in many cancers. Loss of heterozygosity
272 of chr8p frequently occurs in breast and prostate cancers[42,43]. Amplification of chr20q is associated
273 with many cancer types such as pancreatic, gastric, colon, ovarian, cervical, and breast cancers[44].
274 Arm level deletion of chr13q, which includes the *RB1* gene, is associated with neuroendocrine
275 prostate cancer[45]. The CRPC-SCL-enriched/depleted complex rearrangements identified in this study
276 also represent large-scale chromosomal rearrangements. For example, the complex rearrangements
277 spanning *MOB1B*, ranging from 9Mb to 190Mb, cover ~48% of the chromosome on average (fig. 6B).
278
279 Such complex SVs are characteristic of prostate cancer genomes[14,22,46], however it is generally hard
280 to confidently identify true positive events using short-read sequencing alone. Thus, we leveraged the
281 matched Hi-C and tissue RNA-seq data (n=55) to evaluate 3D chromosome conformation of each
282 sample together with its molecular state[18,47]. In the Hi-C contact map, topologically associated
283 domains (TADs) manifest as large genomic regions with elevated internal 3D conformation

interactions, whereas SVs manifest as interactions isolated to the breakpoints and their immediate surrounding regions only[18]. Thus, Hi-C data can be used to validate the SVs, besides inferring their impact on chromatin conformation[48].

We first sought evidence for the complex rearrangements on chromosome 4 spanning *MOB1B* and enriched in CRPC-SCL samples from matched Hi-C data. Towards this end, we looked at the contact strength in the Hi-C map at the locus that stores the interaction between the two breakpoints of the complex rearrangement, referred to as the breakpoint junction (fig. 6A). Assuming the event is true, we expect increased interactions at the breakpoint junction relative to surrounding regions, since regions that are far away from each other in the reference genome are now close by in the tumor genome due to the rearrangement. Indeed, we observe higher contact strength at the breakpoint junction and a reduction of contact strength in its surrounding bins, whereas randomly selected control regions of the same length show no such increase (fig. 6A). Similarly, the complex rearrangements enriched in non-CRPC-SCL samples on chromosome 3 spanning *TAZ* are also supported by increased interactions at breakpoint junctions in those samples (fig. S8A). Furthermore, concordant breakpoints identified separately in matched tissue and cfDNA provide further support for these rearrangements (fig. 6B,C).

We next investigated a potential functional role of the rearrangements in regulating CRPC-SCL. We expected that genes affected by complex rearrangements may have decreased access to their cis-regulatory elements such as enhancers since *MOB1B* shows lower expression in CRPC-SCL samples relative to non-CRPC-SCL (fig. S3E). We analyzed 0.5 Mb region spanning *MOB1B* and find that the strength of 3D contacts, averaged across samples, is lower in CRPC-SCL samples with the rearrangements when compared to those without it (fig. 6B,C,D). By overlaying H3K27ac and ATAC-seq marks with Hi-C contacts, we find that CRPC-SCL samples with the rearrangement show reduced number and contact strength for enhancers connected to *MOB1B* promoter (fig. 6E,F). These trends were reproduced for *TAZ* in non-CRPC-SCL samples (fig. S8). These findings suggest that the complex rearrangements may be associated with *MOB1B* and *TAZ* downregulation at the transcriptional level by reducing promoter access to their enhancers, in addition to their regulation by phosphorylation at the proteomic levels[41]. Even though the breakpoints of rearrangements are far from *MOB1B* and *TAZ* promoters and enhancers, previous studies have shown that large SVs may have a long-distance effect through their impact on the 3D spatial architecture of the chromatin[49]. In line with this, we expect that these rearrangements may also be associated with disruption of other TADs on the chromosome besides the ones surrounding the genes in question. Indeed, by using samples without presence of CRPC-SCL or complex rearrangements as reference, we find that CRPC-SCL samples with the rearrangements have overall fewer conserved TADs than the samples without the rearrangements (fig. S8B).

Logistic regression model to predict CRPC-SCL using genomic alterations

Besides the *MOB1B*, *TAZ*, and *LATS1* variants discussed above, we checked if overall the genomic alterations in the YAP/TAZ pathway are subtype-specific enough to enable identification of CRPC-SCL subtype. Towards this end, we trained a logistic regression model to classify samples containing CPRC-SCL based on alteration events in the YAP/TAZ pathway. The input to the method is the presence or absence of genomic alterations for each gene of the pathway and the output is the probability that the sample exhibits presence of CRPC-SCL subtype. Using Monte Carlo Cross Validation and L1 regularization with a manual parameter search to find the optimal number of features and lambda value for each fold, we classified samples as CRPC-SCL with an accuracy of 0.79 and area under the receiver operating characteristic curve (AUROC) of 0.78, averaged across folds (fig. 5E). These results show that these genomic events are predictive of CRPC-SCL.

CRPC subtypes and genomic heterogeneity and instability

Chromosomal instability and heterogeneity, measured by loss or rearrangement of chromosomes has been reported as a hallmark of cancer and is associated with high disease burden, treatment failure, metastatic progression, and death[50]. Chromosomal instability can be described numerically (i.e. the number of copies of whole chromosomes) or structurally (i.e. the fraction of each chromosome altered)[51,52]. Here, we quantify chromosomal instability as the fraction of the genome altered (FGAlt) by a copy number or structural variant event. We observe that CRPC-SCL samples are enriched for very high FGAlt (fig. 7A,7B). It is possible that high FGAlt may partly contribute to the shorter survival of patients with CRPC-SCL, as it is also associated with aggressive disease in castration-sensitive prostate cancer[53] (fig. 2C).

We have shown that samples with lineage plastic subtypes tend to be more heterogeneous for the presence of multiple subtypes (fig. 3). Because many genomic events are early cancer events and are associated with different molecular states, we expect genomic and epigenomic heterogeneity to relate. Epigenomic heterogeneity refers to the diversity of CRPC subtype composition within a given sample. Genomic heterogeneity refers to the diversity in tumor clone composition within a given sample. Genomic clones are estimated for each sample by HATCHet, the clone-specific copy number caller we used to estimate genome-wide CNAs[54]. CNAs are especially useful in identifying genomic clones because they occur at large scales, often affecting considerable genomic regions, and can be called in an allele-specific manner. We used clone-specific CNAs to construct a genomic heterogeneity score to account for the number of tumor clones, as well as the similarity between them. The score is defined as $n \times (1 - JI)$, where n is the number of tumor clones, and JI is the Jaccard index between clones. We find that lineage plastic samples also show higher genomic heterogeneity scores, which is positively correlated with the number of epigenomic subtypes (Spearman R = 0.22, P = 2.37e-02, fig. 7A,C). Because just the number of subtypes may not fully capture the epigenomic heterogeneity, we assigned an intra-sample epigenomic heterogeneity score to each sample that measures the diversity of the CRPC fraction composition. The score is defined by the normalized Shannon entropy of the subtype fractions, such that a sample entirely comprised of one CRPC subtype would have a score of 0, and a sample comprised of equal parts of all four CRPC subtypes would have a score of 1. Indeed, we observe that genomic heterogeneity is positively correlated with epigenomic heterogeneity (Spearman R = 0.21, P = 3.36e-02).

Discussion

In this study we annotate the epigenomic subtypes of CRPC patient samples using nucleosomal profiling (cfDNA) and transcriptomic (tissue) data. We find that the histologic classifications of adenocarcinoma and neuroendocrine do not capture the intra- and inter-sample subtype heterogeneity, potentially missing important molecular information relevant for therapeutic decisions. Overall, we find that higher subtype heterogeneity is also associated with higher genomic heterogeneity, and CRPC-SCL samples tend to show higher genomic instability as measured by FGAlt. Enrichment of CRPC-SCL tumors in bone biopsies highlights the importance of studying the tumor immune microenvironment of this subtype in future since bone is the most common site of prostate cancer metastasis. We validate our subtype fraction estimations with scRNA-seq and confirmed that non-tumor cells do not confound our calculations[8,30,39]. By relating the genomic events from WGS with the epigenomic subtypes, we find novel genomic alterations at the YAP/TAZ pathway genes that are associated with the CRPC-SCL subtype. The breakpoints of these rearrangements are validated by Hi-C reads. Indeed, by combining all putative functionally disrupting events in the YAP/TAZ pathway, we are able to predict the presence of CRPC-SCL in a given sample with a high accuracy of 0.79 using a logistic regression model.

380 Previously, few genomic alterations such as *RB1* loss were known to be associated with lineage
381 plasticity in CRPC, and our study adds more genomic events to this list. Interestingly, we find the
382 regression model for CRPC-SCL prediction trained on cfDNA WGS samples outperforms the one
383 trained with tissue samples (RNA-seq and WGS), potentially due to higher fraction of cfDNA samples
384 that exhibit high fraction of CRPC-SCL in cfDNA in our cohort.
385
386 It is well known that alterations affecting non-coding regions of the genome (e.g. enhancers) can play
387 a major role in cancer[55]. In prostate cancer, *AR* enhancer amplifications and fusion of the 5' *TMPRSS2*
388 UTR to *ERG* are well studied[14,56]. Large complex rearrangements that span the entire gene or multiple
389 genes have generally been harder to interpret. The availability of matched Hi-C data from patient
390 samples with RNA-seq and WGS allowed us to analyze the enhancer—promoter contacts in samples
391 with versus without rearrangements. Our findings point to potential dysregulation of *MOB1B* by
392 rearrangements on chromosome 4 associated with presence of CRPC-SCL, and of *TAZ* on
393 chromosome 3 associated with absence of CRPC-SCL. While Hi-C data provides support for putative
394 functional roles of these SVs, future studies will be needed to establish the mechanism of their action
395 of gene disruption as well as their role in up- or down-regulation of the YAP/TAZ pathway and lineage
396 plasticity.
397
398 We have shown that both tissue RNA-seq and cfDNA WGS can be used to infer the molecular CRPC
399 subtypes and generally provide consistent results. This is especially impactful since cfDNA is minimally
400 invasive and can be used for serial monitoring. Interestingly, unlike previous observations for genomic
401 heterogeneity where cfDNA exhibits more heterogeneity than tissue, we generally did not observe this
402 trend for epigenomic subtype heterogeneity (fig. S9A)[15]. This observation is also supported by another
403 work using spatial gene expression profiling in which the authors found concordance in gene
404 expression and phenotype classification between metastases from the same individual, albeit with
405 exceptions[11]. However, this observation of absence of higher epigenomic heterogeneity in cfDNA
406 relative to tissue could also be partly due to the limitations of using cfDNA for mixed subtypes inference.
407 Thus, we estimated the limit of detection of the current computational approach to infer CRPC subtype
408 fractions from cfDNA. Under the assumption that each metastatic site sheds cfDNA from molecular
409 subtypes in proportion to their presence in tissue, we find that a subtype fraction of ≤ 0.2 in tissue
410 cannot be detected in cfDNA (fig. S9). These metrics can serve as a guide for the clinical use of cfDNA
411 WGS for molecular subtype inference and guide the further development of computational approaches
412 for subtype inference. Overall, our study provides a framework to move beyond histological
413 classifications of patient tumors to epigenetic subtyping using a clinically feasible assay of cfDNA WGS
414 and shows that it can be used beyond biomarker for discovery of novel genomic alterations associated
415 with lineage plasticity.

416 **Methods**

417 **Cohort Overview**

418 We sequenced cfDNA from 20 patients with CRPC. By combining this with published data, we have
419 amassed a cohort of 488 patients with metastatic CRPC. cfDNA and tissue were collected from 68 and
420 455 patients, respectively, 23 of which were time matched (fig. 1A) (table S1)[8,14,15,18,19,47].
421
422 We analyzed cfDNA WGS from 95 cfDNA samples from 68 patients. 61 samples were from a previously
423 published study[15], which were enriched for adenocarcinoma patients with only 2 patients showing
424 neuroendocrine histology. Thus, we sequenced 20 patient samples from WCM and MSK, out of which
425 8 showed neuroendocrine histology. For some of these patients, we also generated RNA-seq (n=8)
426 and WGS (n=5) data from matched tissue. Additionally, we sequenced 14 samples from patients with

427 no cancer, as controls. cfDNA samples in Herberts et al. were collected from patients at clinically
428 relevant timepoints, such that patients had either 1 (n = 14), 2 (n = 13), or 3 (n = 7) cfDNA samples in
429 total[15]. Tumor fraction ranged from 0.11 to 0.92 across samples (mean = 0.46, median = 0.45)[57]. Mean
430 coverage achieved across samples ranged from 8.64X to 182.39X (mean = 87.57X, median = 102.17X)
431 (fig. 1B) (table S1). 32,444 structural variants (SVs) were identified across all samples, with a mean of
432 421.35 SVs per sample (range: 17 – 1,086). 2,165,361 single nucleotide variants (SNVs) were identified
433 across all samples, with a mean of 5,217 non-intergenic, annotated SNVs per sample (range: 15 –
434 59,738).
435
436 Tissue RNA-seq, WGS, and Hi-C datasets from 482, 105, and 55 samples, respectively were analyzed
437 [8,14,18,19,21]. 514, 71, and 327 samples from patients with adenocarcinoma, neuroendocrine, and poorly
438 differentiated/inadequate for diagnosis/not available histologies, respectively. Out of these 123 samples
439 were from WCM and 789 were from other published studies[8,14,18,19,47]. Tissue samples were collected
440 from various metastatic sites including soft tissue (n = 71), lymph node (n = 336), bone (n = 263),
441 bladder (n = 2), prostate (n = 19), lung (n = 15), brain (n = 9), liver (n = 122), skull base (n = 1), ureter
442 (n = 1), adrenal (n = 3), mediastinum (n = 1), spine (n = 1), epidural thoracic (n = 1), and intercostal (n
443 = 1) (table S1).
444

445 **cfDNA WGS**

446 *Patient samples from WCM and MSK*

447 Fresh blood or frozen plasma samples from consented prostate cancer patients were collected under
448 Weill Cornell Medicine Institutional Review Board approval 20-04021962 prior to sample acquisition.
449 Patient blood was collected in Streck tubes and spun at 1600xg for 15 min at 25ºC. The plasma was
450 decanted from the top fraction of the Streck tube and cfDNA was isolated immediately if possible, or
451 frozen at -80ºC. Plasma cfDNA was isolated using the NeoGeneStar cfDNA variable volume kit
452 according to manufacturer's instructions. For germline DNA, we took the top 2ml of the remaining red
453 blood cell component of the sample from the Streck tube, added 4ml RPMI-1640, mixed gently,
454 underlayered with 3ml Histopaque 1.077, spun 400xg for 30 min., room temperature, with no break,
455 and isolated the peripheral blood mononuclear cells (pbmcs) from the interface. DNA from the pbmcs
456 was isolated using the Qiagen DNeasy Blood and Tissue Kit according to manufacturer's instructions.
457 All samples were quantitated on Qubit HS and frozen at -80ºC. Library preparation and WGS were
458 performed at the New York Genome Center using the Kapa Hyper PCR+ cfDNA on the Illumina
459 NovaSeq with 150 paired-end reads and coverages of 0.1, 10, 40 or 80X. Library quality was verified
460 using Agilent Bioanalyzer 2100 and Qubit.
461
462 The raw data was aligned to hg38 using BWA mem (version 0.7.15) with parameters -Y -K 100000000
463 -t 8. Base quality scores were adjusted using GATK ApplyBQSR (version 4.1.0.0).

464 *Publicly available patient samples*

465 Raw data was downloaded from the European Genome-Phenome Archive (EGAS00001005783).
466 Fastqs were aligned to hg38 using BWA mem (version 0.7.17) with parameters -M -t 20.

467 *Publicly available PDX samples*

468 Raw data was downloaded from NCBI BioProject (PRJNA900550)[10]. Fastqs were aligned to hg38 and
469 mouse reads were removed using the same pipeline described in De Sarkar and Patton et al[10].

470 **ATAC-seq**

471 *Human PBMCs*

472 Fresh PBMCs were collected from a healthy control WCM sample and processed according to the
473 Omni-ATAC protocol in Corces et. al[58]. The partially tagmented samples were sent to the WCM
474 Epigenomics Core for the remainder of the library prep (Illumina) and P2 100 cycles run on
475 NextSeq2000.
476
477 Fastqs were aligned to the hg38 reference using BWA mem (version 0.7.15) with parameters -t 6 -M -
478 a -h 100 -L 50,50 and -O 7. Open chromatin peaks were called using genrich (version v0.6.1,
479 https://github.com/jsh58/Genrich) with parameters -j -d 50 -r -e chrM -p 0.01 -q 0.05 -a 20 -g 20 -l 100
480 -v. IDR (version v2.0.4.2, https://github.com/nboley/idr) was used to get consensus peaks across
481 technical replicates with parameters --output-file-type narrowPeak --rank p.value --plot --use-best-
482 multisummit-IDR --verbose.
483

484 *Publicly available mouse PDX samples*

485 Publicly available LuCaP ATAC-seq data was downloaded from GEO (GSE156292)[10]. Fastqs were
486 aligned to hg38 using bowtie2 (version 2.4.1) with parameters --wrapper basic-0 -k 10 -t -p 16. Open
487 chromatin peaks were called using genrich (version 0.6.1) with parameters -t -j -v -r -q 0.05 -l 100 and
488 -E to exclude gaps, patches, centromeres, alternative haplotypes, centromeres, and black-listed
489 regions.

490 **RNA-Seq**

491 Publicly available tissue RNA-seq was downloaded directly from Tang et al.[8],
492 https://quigleylab.ucsf.edu/data[14,47], and
493 https://github.com/cBioPortal/datahub/raw/refs/heads/master/public/prad_su2c_2019[19].

494 **Tumor fraction**

495 ichorCNA (version 0.3.2, https://github.com/broadinstitute/ichorCNA) with default parameters was used
496 to estimate tumor fraction from WGS cfDNA[57].

497 **Copy number alterations**

498 *cfDNA WGS and matched tissue WGS*

499 HATCHet was used to call copy number alterations from WGS cfDNA and matched tissue (when
500 available)[54]. This applied to the in-house (WCM and MSK) and Herberts, Annala, and Sipola et al[15]
501 cohorts.

502 *Tissue WGS*

503 Copy number alterations were called using CopyCat and downloaded directly from
504 https://quigleylab.s3.us-west-
505 2.amazonaws.com/datasets/2018_04_15_matrix_CN_integer_symbol_copycat.txt.zip. This applied to
506 the SU2C (West Coast) cohort[14].

507 **Structural variant calling**

508 *cfDNA WGS*

509 SVs from publicly available data were retrieved from the authors[15]. To achieve symmetry, we followed
510 the protocol of Herberts et al for our in-house samples (relaxing certain thresholds to match sequencing
511 depth), using Breakfast (version 0.6.0, https://github.com/annalam/breakfast) with parameters --max-

frag-len = 1000 and --anchor-len = 30, requiring at least 5 unique junction-spanning reads[15]. The following thresholds were used to further filter the data: at least 4 mutant reads, at least 4 reads of total depth, VAF ≥ 0.1, average mapping quality of at least 20, and average sidedness (distance to read end) of at least 15.

Tissue WGS

SVs from publicly available data were called using Lumpy and were downloaded directly from https://s3-us-west-2.amazonaws.com/feng.genomics/WGBS/secondary_data.zip[18]. SVs found in more than 4 samples (breakpoint within 10 bps) in the cohort were considered non-unique and removed. SVs that were found in either of two databases of germline variants (dbVar[59] and InvFEST[60]) were removed (breakpoints within 100 bps).

Single nucleotide variant calling

cfDNA WGS

SNVs from publicly available data were retrieved from the authors[15]. To achieve symmetry, we followed the protocol of Herberts, Annala, Sipola et al for our in-house samples, using mutato (version 0.9.0, https://github.com/annalam/mutato) with arguments --alt-reads = 5 --alt-frac = 0.05. Only SNVs with at least 1 supporting read with average mapping quality ≥ 10 and within 15 bp of the read end, VAF ≥ 0.1, and a population allele frequency $< 0.5\%$ (from GNOMAD, version 3.0) were retained[15]. The functional impact of the SNVs was annotated using ANNOVAR (version 20191024) with parameters hg38 regGene gene-based annotation[61].

Tissue WGS

SNVs from publicly available data were called using Strelka and were downloaded directly from https://quigleylab.s3.us-west-2.amazonaws.com/datasets/2018_04_15_WCDT_somatic_vcf.tar[14,18]. The functional impact of the SNVs was annotated using ANNOVAR (version 20191024) with parameters hg38 regGene gene-based annotation[61].

CRPC subtype-specific ATAC-seq peaks

ATAC-seq peaks in CRPC cell lines and organoids were called using genrich (version 0.6.1) with parameters -t -d 50 -e chrM -j -v -r -a 20 -g 20 -q 0.05 -l 100 and -E to exclude gaps, patches, centromeres, alternative haplotypes, centromeres, and black-listed regions. IDR (version 2.0.2) was used to get consensus peaks across replicates with parameters --output-file-type narrowPeak --rank p.value --verbose. Differentially accessible ATAC-seq peaks (DAAPs) generated with macs2 peaks were downloaded from Tang, Xu, Wang, & Wong et al[8]. For every macs2 peak of CRPC subtype A, if there was at least one cell line or organoid of subtype A with an overlapping genrich peak and there were no cell lines or organoids of any other subtype with an overlapping genrich peak, the subtype specific peak was defined by a start (min(start of all genrich peaks of cell lines/organoids of subtype A that overlap the macs2 DAAP)), end (max(end of all genrich peaks of cell lines/organoids of subtype A that overlap the macs2 DAAP)), and summit (int(median(summits of all genrich peaks of cell lines/organoids of subtype A that overlap the macs2 DAAP))). Any peak that overlapped a genrich ATAC-seq peak of our in-house no cancer control sample (ATAC-seq Human PBMCs above) was removed. Overall, there were 11,658 CRPC-AR sites, 13,959 CRPC-SCL sites, 13,732 CRPC-WNT sites, and 11,642 CRPC-NE sites (table S14).

CRPC subtype fraction estimation

cfDNA WGS

We performed deconvolution using Keraon[10]. The signature matrix was built by averaging the WGS cfDNA mean coverage across PDXs of the same CRPC subtype in CRPC subtype-specific accessible

556 chromatin sites of that subtype (table S5). Because we had no CRPC-WNT PDXs, we used a CRPC-
557 WNT patient for the signature and excluded it from other analyses. Features used were central
558 coverage (30 bp window centered at the summit) and window coverage (990 bp window centered at
559 the summit). Signatures were also computed from 14 healthy control samples and were subtracted out
560 of the PDX signature (tables S5,S6). The mixture matrix was the WGS cfDNA mean coverage of each
561 sample in CRPC subtype-specific accessible chromatin sites (fig. S1B).

562 *Tissue RNA-seq*

563 Deconvolution was performed using EPIC[20]. The signature matrix was built based on averaging the
564 expressions (Transcripts Per Million, TPM) across cell lines and organoids of the same CRPC subtype
565 in CRPC signature genes[8] (tables S2,S3). The mixture matrix was the gene expression values (TPM)
566 of each sample for CRPC signature genes[8]. The mixture matrix is then regressed back onto the
567 signature matrix to estimate fractional contributions of each CRPC subtype to each patient's expression
568 profile (fig. S1A).

569 **scRNA-seq analysis**

570 Single-cell RNA-seq count matrices derived from human metastatic CRPC biopsy samples were
571 downloaded directly from GEO (GSE210358)[9]. To perform pseudo-bulking and conversion to TPM,
572 gene counts were summed across all cells in each sample (only common genes across samples
573 were retained). Gene lengths were acquired from a biomaRt query to use in TPM conversion[62]. For
574 tumor-only pseudo-bulking, the same approach was used across only tumor cells (GSM6428952)[9].
575 To annotate these cells, the authors used a hierarchical strategy wherein broad categories of
576 epithelial, immune, and stromal cells were identified using expression of marker genes for these
577 categories. Expression of genes that are known to be upregulated in prostate cancer are used to
578 identify tumor cells. Cell type assignments were confirmed by showing inferred CNVs were higher in
579 tumor cells relative to non-tumor cells[30].
580

581 **Metastatic site enrichment**

582 For each CRPC subtype, we performed a two-tailed Fisher's exact test to determine if the odds of
583 samples from that subtype coming from a particular metastatic site versus others were statistically
584 significant. This analysis was performed on the tissue dataset and was limited to samples with CRPC
585 subtype fraction ≥ 0.5.

586 **Genomic event enrichment**

587 For each comparison, we performed a one-tailed binomial test to determine if the probability of samples
588 from a given group having the alteration was significantly different from the probability of other samples
589 having the alteration. We had segment-level copy number calls for cfDNA and gene-level scalar copy
590 number calls for tissue. For AR amplifications, we checked for amplifications (CN>3 in cfDNA, CN>3 in
591 tissue – values chosen based on CN distribution) in CRPC-AR samples versus others. For biallelic
592 inactivation of RB1, we checked for homozygous deletions (CN≤1.2 in cfDNA, CN≤0.5 in tissue –
593 values chosen based on CN distribution) or a combination of at least two of the following events:
594 heterozygous deletions (1.2≤CN<1.75 in cfDNA, 0.5≤CN<1.6 in tissue – values chosen based on CN
595 distribution), inactivation by SV (i.e. SV breakpoint intersecting gene), stopgain, and splice mutations.
596 For CTNNB1 mutations, they were putative driver missense mutations. Only complex rearrangements
597 that were significant in both cfDNA and tissue were reported.

598 **CRPC-SCL prediction using genomic variants**

599 We trained a logistic regression model to classify samples as CRPC-SCL or not, using a 2:1 train/test
600 split. We performed this 10 times using different seeds each time. We performed L1 regularization with

601 a manual parameter search to find the optimal number of features and lambda value, testing c values
602 within an np.logspace(-4,4,20) for each train/test split. The feature matrix had samples in the rows and
603 YAP/TAZ pathway genes in the columns and was populated by 1 if the sample had events deemed
604 putatively functional (a complex rearrangement, missense (putative driver) mutation, or stopgain
605 mutation of the gene), and 0 otherwise. The target classes were 0 if the sample was not CRPC-SCL
606 and 1 if it was. We checked that including other genomic events did not significantly change the
607 performance of the model.
608
609 We also trained models to classify the other CRPC subtypes, but CRPC-SCL performed the best by
610 far. We hypothesize that classification of CRPC-NE (AUC=0.61, ACC=0.65) and CRPC-WNT
611 (AUC=0.64, ACC=0.64) is better than random because many of the samples also contain CRPC-SCL.

612 **Hi-C analysis**

613 Normalized contact maps were downloaded from GEO (GSE249494)[18]. We leverage the information
614 obtained from the Hi-C experiment in two main tasks. First, the predicted breakpoints were validated
615 using Hi-C interactions by searching the nonlinear contact map. We compare the contact strength at
616 the breakpoint junction to its surrounding regions. We define a search space of 10 Hi-C bins (100 Kb)
617 on each side of the breakpoint junctions. For each sample with the complex rearrangement and the Hi-
618 C contact map available, we calculated the contact values in the search space, aggregated across
619 samples. Then, we evaluate the trend of the aggregated contact strength in the search space by fitting a
620 curve using a smoothing window of two Hi-C bins (20 Kb). As a control, we evaluate the same trends in
621 random regions to show that nonlinear interactions at the same distance are only seen due to
622 breakpoints (fig. 6A). Secondly, we assessed the functional effect of the rearrangements on the Hi-C
623 interactions at genomic regions associated with the CRPC-SCL subtype transition and the impact on
624 enhancer-promoter interactions. We evaluated the average strength per contact within 500 Kb TADs
625 harboring the YAP/TAZ inhibitor, MOB1B, using CRPC-SCL samples with and without the
626 rearrangement (fig. 6C,D). We reproduced these trends in YAP/TAZ activator, TAZ, in Non-CRPC-SCL
627 samples (fig. S8). Enhancer regulatory regions were then defined by the overlap of in-house generated
628 ATAC-seq peaks[8] and DU145 H3K27ac marks downloaded from
629 https://figshare.com/articles/dataset/H3K27ac_Signal_Track_for_DU145/12442796. Thus, we further
630 verified the specific change in the average strength of enhancer-promoter connections between SCL
631 samples with and without the rearrangements (fig. 6E,F, S6C).

632 **Epigenomic and genomic heterogeneity scores**

633 The epigenomic heterogeneity score is the Shannon entropy of the subtype fractions, normalized by
634 the number of possible CRPC subtypes (i.e. 4) to restrict the range from 0 to 1 (table S15).
635
636 The genomic heterogeneity score is $\#\ genomic\ clones\ \times (1 - Jaccard\ index\ between\ clones)$ where
637 the Jaccard index was 1 for samples with only one clone (table S15).

638 **Fraction of genome altered**

639 Fraction of genome altered is the sum of CNA segment lengths with abnormal copy number in at least
640 one clone intersected with SVs (excluding interchromosomal translocations) divided by the length of
641 the genome (table S16). We find that high FGAlt (>0.85) is enriched in CRPC-SCL. This trend is the
642 same across thresholds (fig. S10). We find that CNAs are the largest contributor to FGAlt.

643 **Survival analysis**

644 We generated Kaplan-Meier curves using progression free survival in units of days as the measure of
645 time. Every event was counted as progression. We performed a one-tailed log rank test to determine if
646 the curves were statistically different from one another (fig. 2C).

Limit of detection

We compared CRPC subtype fractions in tissue RNA-seq and cfDNA WGS in patients for whom we have matched data (fig. S9A). We performed in-silico simulations to estimate our limit of detection with respect to the fraction of CRPC subtype present, the tumor fraction of the sample, and the average sequencing coverage of the sample.

Subtype fraction

To estimate the lowest fraction of CRPC subtype detectable from cfDNA, we chose patient AE-180 as a model. At baseline, we estimated he was 100% CRPC-AR (tumor fraction = 0.4718, mean coverage = 111.1X). At progression2, however, he was 100% CRPC-NE (tumor fraction = 0.614, mean coverage = 69.67X). By mixing specific amounts of AE-180-Baseline with AE-180-Progression2 and a healthy control, we were able to create a sample with a target CRPC-AR fraction, while maintaining a fixed coverage (40X) and tumor fraction (0.4718), the tumor fraction of AE-180-Baseline without mixing. For each target CRPC-AR fraction, we repeated the experiment 100 times, each with a different seed, generating a distribution of estimated CRPC-AR fractions across experiments. By assuming the target CRPC-AR fraction as ground truth, we evaluated our statistical and systematic errors in estimating subtype fractions. The statistical error was never more than 2.1% across target CRPC-AR fractions (fig. S9B). When the CRPC subtype fraction is less than 0.3, we do not detect it at all. When it is close to this limit, our systematic error is high, and we underestimate the contribution of the small subtype.

We compute the fractions of AE-180-Baseline, AE-180-Progression2, and control required for mixing to achieve the desired target CRPC-AR and CRPC-NE fraction as follows: We define three samples S_1, S_2, and S_3 with CRPC-AR fraction F_1, F_2, and F_3, tumor fraction T_1, T_2, and T_3 and coverage C_1, C_2, and C_3 such that $T_1 \neq T_2 \neq T_3$ and $C_1 \neq C_2 \neq C_3$. Let S_3 be the healthy sample such that $T_3 = 0$. Our target mixed sample is S_4, such that $T_4 = \frac{a_1T_1C_1+a_2T_2C_2+a_3T_3C_3}{a_1C_1+a_2C_2+a_3C_3}$ and $C_4 = a_1C_1 + a_2C_2 + a_3C_3$, for some constants a_1, a_2, and a_3. This relies on the assumption that every sample is made up of some (potentially zero) tumor and healthy component such that $S_i = S_i^T + S_i^H$, $T_i = T_i^T + T_i^H$, and $C_i = C_i^T + C_i^H$. Then $T_4 = \frac{a_1T_1C_1+a_2T_2C_2+a_3T_3C_3}{a_1C_1+a_2C_2+a_3C_3} = \frac{C_4^T}{C_4}$. And $a_1C_1 + a_2C_2 + a_3C_3 = C_4$, $a_1T_4C_1 + a_2T_4C_2 + a_3T_4C_3 = a_1T_1C_1 + a_2T_2C_2 + a_3T_3C_3$, and $C_1(T_4 - T_1)a_1 + C_2(T_4 - T_2)a_2 + C_3(T_4 - T_3)a_3 = 0$. Also, $(a_1T_1C_1 + a_2T_2C_2 + a_3T_3C_3)F_4 - (a_1T_1C_1F_1 + a_2T_2C_2F_2 + a_3T_3C_3F_3) = 0$, and $(a_1T_1C_1)(F_4 - F_1) + (a_2T_2C_2)(F_4 - F_2) + (a_3T_3C_3)(F_4 - F_3) = 0$. Thus, we solve the following linear equation to solve for fractions a_1, a_2, and a_3: $\begin{bmatrix} C_1 & C_2 & C_3 \\ C_1(T_4 - T_1) & C_2(T_4 - T_2) & C_3(T_4 - T_3) \\ T_1C_1(F_4 - F_1) & T_2C_2(F_4 - F_2) & T_3C_3(F_4 - F_3) \end{bmatrix} \times \begin{bmatrix} a_1 \\ a_2 \\ a_3 \end{bmatrix} = \begin{bmatrix} C_4 \\ 0 \\ 0 \end{bmatrix}$.

Statistical error was estimated by the standard deviation of CRPC-AR fraction across 100 runs of a given target (CRPC-AR, CRPC-NE) fraction pair. Systematic error was estimated by the difference between the mean CRPC-AR fraction across 100 runs of a given target (CRPC-AR, CRPC-NE) pair and the actual CRPC-AR fraction of the sample without mixing.

Tumor fraction and coverage

To estimate our ability to accurately detect CRPC subtype fraction from cfDNA with respect to coverage and tumor fraction, we chose sample AE-092-Baseline (coverage = 17.18X, tumor fraction = 0.78), who had a CRPC-SCL fraction of 0.43, as a model. We chose this sample because of its high tumor fraction and relatively high CRPC-SCL fraction. By downsampling and mixing specific amounts of AE-092-Baseline with a healthy control, we were able to create a sample with a target coverage and tumor fraction combination. For each target coverage, tumor fraction pair, we repeated the experiment 100 times, each with a different seed, generating a distribution of estimated CRPC-SCL fractions across

experiments. By assuming the CRPC-SCL fraction without downsampling or mixing – i.e. 0.43 – as ground truth, we evaluated our statistical and systematic errors in estimating subtype fractions. Statistical error stems from having fixed, finite coverage and can be estimated by the standard deviation of CRPC-SCL fraction estimates across the 100 experiments. Although the statistical error goes up with lower coverage and tumor fraction, it remains below 5% for coverage down to 3X and tumor fraction down to 0.1. Using these experiments as a template, we estimated the statistical errors on each of our patient samples using their coverage and tumor fraction. On average, the statistical error of the cohort was 1.3% (fig. S9C). We find that the systematic error is mostly independent of coverage but increases with lower tumor fraction and remains around 6% or below for tumor fraction down to 0.1. Using these experiments as a template, we estimated the systematic errors on each of our patient samples using their coverage and tumor fraction. On average, the systematic error was 1.5% (fig. S9D). Calculations were performed similarly to estimating limit of detection of subtype fraction above.

Data Availability

Processed data is provided in supplemental tables. Raw data will be made available after publication.

Acknowledgements

We thank the Khurana and Chen lab members for their input and discussion. We are grateful to the Englander Institute for Precision Medicine for WCM CRPC patient samples, including Alexandria Norton, Christina Federov, John Mills, and John Otilano for their facilitation. We also thank the WCM Genomics Core and Epigenomics Core facilities.

Funding

S.EN. thanks the National Institutes of Health (R25CA233208) for their support. M.R. thanks the National Institutes of Health (T32 GM083937) for their support**.** T.A.G. was supported by a Medical Scientist Training Program grant from the National Institute of General Medical Sciences of the National Institutes of Health under award number**:** T32GM152349 to the Weill Cornell/Rockefeller/Sloan Kettering Tri-Institutional MD-PhD Program. E.K. thanks the National Institutes of Health (R01CA218668 and P50CA211024), the Department of Defense (HT9425-23-1-0074), the Ann and William Bresnan Foundation, and the WorldQuant Foundation for their support.

Author Contributions

M.R., A.M.F., and E.K. conceived of and designed the project. M.R., A.M.F., and E.K. wrote the manuscript with the help of all authors. M.R. and A.M.F. performed the majority of the data analysis. S.C. performed cfDNA sample preparation for WGS. M.M., M.B. and B.J.R. redesigned HATCHet for cfDNA WGS. W.L., A.B.T., T.A.G., S.EN., R.B., P.D., and K.G. helped with data analysis. J.M.M., B.D.R., M.A., and M.AA. performed pathological review. M.S., J.M., S.T., D.N., A.M., J.N., C.N.S., J.M., and A.S. managed and coordinated WCM data and sample delivery. E.B., H.I.S., and Y.C., managed and coordinated MSK data and sample delivery. B.J.R. and Y.C. helped supervise the study. E.K. supervised the study.

References

1. Chi, K. N. *et al.* Apalutamide for metastatic, castration-sensitive prostate cancer. *New England Journal of Medicine* **381**, (2019).
2. Fizazi, K. *et al.* Abiraterone plus Prednisone in Metastatic, Castration-Sensitive Prostate Cancer. *New England Journal of Medicine* **377**, 352–360 (2017).

3. Davis, I. D. *et al.* Enzalutamide with Standard First-Line Therapy in Metastatic Prostate Cancer. *New England Journal of Medicine* **381**, 121–131 (2019).
4. James, N. D. *et al.* Abiraterone for Prostate Cancer Not Previously Treated with Hormone Therapy. *New England Journal of Medicine* **377**, 338–351 (2017).
5. Watson, P. A., Arora, V. K. & Sawyers, C. L. Emerging mechanisms of resistance to androgen receptor inhibitors in prostate cancer. *Nat Rev Cancer* **15**, 701–711 (2015).
6. Bluemn, E. G. *et al.* Androgen Receptor Pathway-Independent Prostate Cancer Is Sustained through FGF Signaling. *Cancer Cell* **32**, 474-489.e6 (2017).
7. Labrecque, M. P. *et al.* Molecular profiling stratifies diverse phenotypes of treatment-refractory metastatic castration-resistant prostate cancer. *Journal of Clinical Investigation* **129**, 4492–4505 (2019).
8. Tang, F. *et al.* Chromatin profiles classify castration-resistant prostate cancers suggesting therapeutic targets. *Science (1979)* **376**, (2022).
9. Chan, J. M. *et al.* Lineage plasticity in prostate cancer depends on JAK/STAT inflammatory signaling. *Science (1979)* **377**, (2022).
10. De Sarkar, N. *et al.* Nucleosome Patterns in Circulating Tumor DNA Reveal Transcriptional Regulation of Advanced Prostate Cancer Phenotypes. *Cancer Discov* **13**, 632–653 (2023).
11. Brady, L. *et al.* Inter- and intra-tumor heterogeneity of metastatic prostate cancer determined by digital spatial gene expression profiling. *Nat Commun* **12**, (2021).
12. Visakorpi, T. *et al.* In vivo amplification of the androgen receptor gene and progression of human prostate cancer. *Nat Genet* **9**, (1995).
13. Viswanathan, S. R. *et al.* Structural Alterations Driving Castration-Resistant Prostate Cancer Revealed by Linked-Read Genome Sequencing. *Cell* **174**, 433-447.e19 (2018).
14. Quigley, D. A. *et al.* Genomic Hallmarks and Structural Variation in Metastatic Prostate Cancer. *Cell* **174**, 758-769.e9 (2018).
15. Herberts, C. *et al.* Deep whole-genome ctDNA chronology of treatment-resistant prostate cancer. *Nature* **608**, 199–208 (2022).
16. Zhou, Z. *et al.* Synergy of p53 and Rb deficiency in a conditional mouse model for metastatic prostate cancer. *Cancer Res* **66**, 7889–7898 (2006).
17. Yu Ku, S. *et al.* Rb1 and Trp53 cooperate to suppress prostate cancer lineage plasticity, metastasis, and antiandrogen resistance. *Science (1979)* **355**, 78–83 (2017).
18. Zhao, S. G. *et al.* Integrated analyses highlight interactions between the three-dimensional genome and DNA, RNA and epigenomic alterations in metastatic prostate cancer. *Nat Genet* **56**, (2024).
19. Abida, W. *et al.* Genomic correlates of clinical outcome in advanced prostate cancer. *PNAS* **116**, (2019).
20. Racle, J. ; G. D. EPIC: A Tool to Estimate the Proportions of Different Cell Types from Bulk Gene Expression Data. in *Bioinformatics for Cancer Immunotherapy: Methods and Protocols* (ed. Boegel, S.) 233–248 (Springer US, 2020). doi:10.1007/978-1-0716-0327-7_17.
21. Zhao, S. G. *et al.* The DNA methylation landscape of advanced prostate cancer. *Nat Genet* **52**, 778–789 (2020).
22. Zhou, M. *et al.* Patterns of structural variation define prostate cancer across disease states. *JCI Insight* **7**, (2022).
23. van Dessel, L. F. *et al.* The genomic landscape of metastatic castration-resistant prostate cancers reveals multiple distinct genotypes with potential clinical impact. *Nat Commun* **10**, (2019).
24. Khani, F. *et al.* Evolution of structural rearrangements in prostate cancer intracranial metastases. *NPJ Precis Oncol* **7**, (2023).
25. Li, Y. *et al.* Patterns of somatic structural variation in human cancer genomes. *Nature* **578**, 112–121 (2020).

783 26. Snyder, M. W., Kircher, M., Hill, A. J., Daza, R. M. & Shendure, J. Cell-free DNA Comprises an
784 in Vivo Nucleosome Footprint that Informs Its Tissues-Of-Origin. *Cell* **164**, 57–68 (2016).
785 27. Abeshouse, A. *et al.* The Molecular Taxonomy of Primary Prostate Cancer. *Cell* **163**, 1011–
786 1025 (2015).
787 28. Mu, P. *et al.* SOX2 promotes lineage plasticity and antiandrogen resistance in TP53-and RB1-
788 deficient prostate cancer. *Science (1979)* **355**, 84–88 (2017).
789 29. Beltran, H. *et al.* Divergent clonal evolution of castration-resistant neuroendocrine prostate
790 cancer. *Nat Med* **22**, 298–305 (2016).
791 30. Zaidi, S. *et al.* Single-cell analysis of treatment-resistant prostate cancer: Implications of cell
792 state changes for cell surface antigen–targeted therapies. *Proc Natl Acad Sci U S A* **121**,
793 (2024).
794 31. Beltran, H. *et al.* The role of lineage plasticity in prostate cancer therapy resistance. *Clinical*
795 *Cancer Research* **25**, 6916–6924 (2019).
796 32. Steeg, P. S. Tumor metastasis: Mechanistic insights and clinical challenges. *Nat Med* **12**, 895–
797 904 (2006).
798 33. Horak, C. E. & Steeg, P. S. Metastasis gets site specific. *Cancer Cell* **2**, (2005).
799 34. Chen, W., Hoffmann, A. D., Liu, H. & Liu, X. Organotropism: new insights into molecular
800 mechanisms of breast cancer metastasis. *NPJ Precis Oncol* **2**, (2018).
801 35. Aggarwal, R., Zhang, T., Small, E. J. & Armstrong, A. J. Neuroendocrine Prostate Cancer:
802 Subtypes, Biology, and Clinical Outcomes. *J Natl Compr Canc Netw* **12**, (2014).
803 36. Sipola, J. *et al.* Plasma cell-free DNA chromatin 1 immunoprecipitation profiling depicts
804 phenotypic and 2 clinical heterogeneity in advanced prostate cancer. *Cancer Res* (2024).
805 37. Datta, K., Muders, M., Zhang, H. & Tindall, D. J. Mechanism of lymph node metastasis in
806 prostate cancer. *Future Oncology* **6**, 823–836 (2010).
807 38. Su, W. *et al.* The Polycomb Repressor Complex 1 Drives Double-Negative Prostate Cancer
808 Metastasis by Coordinating Stemness and Immune Suppression. *Cancer Cell* **36**, 139-155.e10
809 (2019).
810 39. Kfoury, Y. *et al.* Human prostate cancer bone metastases have an actionable
811 immunosuppressive microenvironment. *Cancer Cell* **39**, 1464-1478.e8 (2021).
812 40. Mohyeldin, A., Garzón-Muvdi, T. & Quiñones-Hinojosa, A. Oxygen in stem cell biology: A
813 critical component of the stem cell niche. *Cell Stem Cell* **7**, 150–161 (2010).
814 41. Wang, Y. *et al.* Comprehensive Molecular Characterization of the Hippo Signaling Pathway in
815 Cancer. *Cell Rep* **25**, 1304-1317.e5 (2018).
816 42. Anbazhagan, R., Fujii, H. & Gabrielson, E. *Allelic Loss of Chromosomal Arm 8p in Breast*
817 *Cancer Progression*. *American Journal of Pathology* vol. 152 (1998).
818 43. Kluth, M. *et al.* Deletion of 8p is an independent prognostic parameter in prostate cancer.
819 *Oncotarget* **8**, 379–392 (2017).
820 44. Kimura, Y. *et al.* Genetic alterations in 102 primary gastric cancers by comparative genomic
821 hybridization: Gain of 20q and loss of 18q are associated with tumor progression. *Modern*
822 *Pathology* **17**, 1328–1337 (2004).
823 45. Melamed, J., Einhorn, J. M. & Ittmann2, M. M. Allelic loss on chromosome 13q in human
824 prostate carcinoma. *Clin Cancer Res* **3**, 1867–1872 (1997).
825 46. Berger, M. F. *et al.* The genomic complexity of primary human prostate cancer. *Nature* **470**,
826 214–220 (2011).
827 47. Lundberg, A. *et al.* The Genomic and Epigenomic Landscape of Double-Negative Metastatic
828 Prostate Cancer. *Cancer Res* **83**, 2763–2774 (2023).
829 48. Song, F., Xu, J., Dixon, J. & Yue, F. Analysis of Hi-C Data for Discovery of Structural Variations
830 in Cancer. in *Hi-C Data Analysis; Methods and Protocols* (eds. Bicciato, S. & Ferrari, F.) 143–
831 161 (Humana, 2021).

832 49. Shanta, O. *et al.* The effects of common structural variants on 3D chromatin structure. *BMC*
833 *Genomics* **21**, (2020).
834 50. Hanahan, D. & Weinberg, R. A. Hallmarks of cancer: The next generation. *Cell* **144**, 646–674
835 (2011).
836 51. Vargas-Rondón, N., Villegas, V. E. & Rondón-Lagos, M. The role of chromosomal instability in
837 cancer and therapeutic responses. *Cancers (Basel)* **10**, (2018).
838 52. Bayani, J. *et al.* Genomic mechanisms and measurement of structural and numerical instability
839 in cancer cells. *Semin Cancer Biol* **17**, 5–18 (2007).
840 53. Stopsack, K. H. *et al.* Oncogenic genomic alterations, clinical phenotypes, and outcomes in
841 metastatic castration-sensitive prostate cancer. *Clinical Cancer Research* **26**, 3230–3238
842 (2020).
843 54. Zaccaria, S. & Raphael, B. J. Accurate quantification of copy-number aberrations and whole-
844 genome duplications in multi-sample tumor sequencing data. *Nat Commun* **11**, (2020).
845 55. Khurana, E. *et al.* Role of non-coding sequence variants in cancer. *Nat Rev Genet* **17**, 93–108
846 (2016).
847 56. Tomlins, S. A. *et al.* Recurrent Fusion of TMPRSS2 and ETS Transcription Factor Genes in
848 Prostate Cancer. *Science (1979)* **310**, (2005).
849 57. Adalsteinsson, V. A. *et al.* Scalable whole-exome sequencing of cell-free DNA reveals high
850 concordance with metastatic tumors. *Nat Commun* **8**, (2017).
851 58. Corces, M. R. *et al.* An improved ATAC-seq protocol reduces background and enables
852 interrogation of frozen tissues. *Nat Methods* **14**, 959–962 (2017).
853 59. Phan, L. *et al.* dbVar structural variant cluster set for data analysis and variant comparison.
854 *F1000Res* **5**, 673 (2016).
855 60. Martínez-Fundichely, A. *et al.* InvFEST, a database integrating information of polymorphic
856 inversions in the human genome. *Nucleic Acids Res* **42**, (2014).
857 61. Wang, K., Li, M. & Hakonarson, H. ANNOVAR: Functional annotation of genetic variants from
858 high-throughput sequencing data. *Nucleic Acids Res* **38**, (2010).
859 62. Harrison, P. W. *et al.* Ensembl 2024. *Nucleic Acids Res* **52**, D891–D899 (2024).

860

861

A

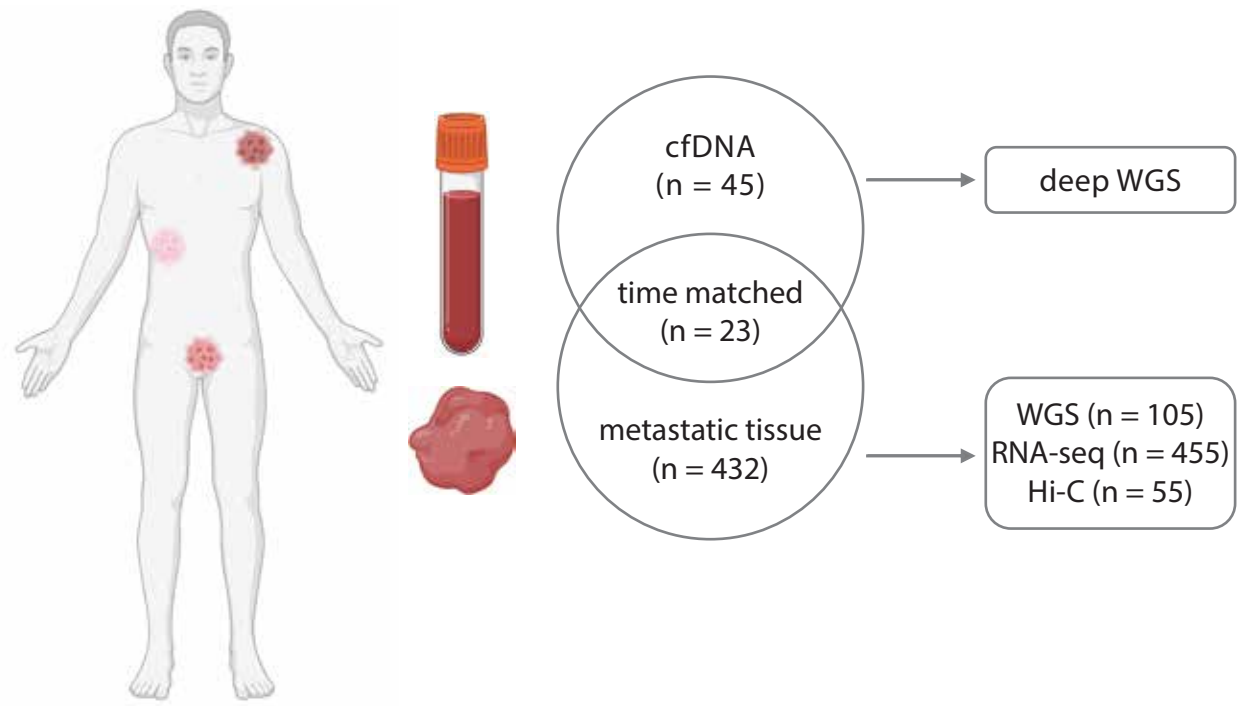

B

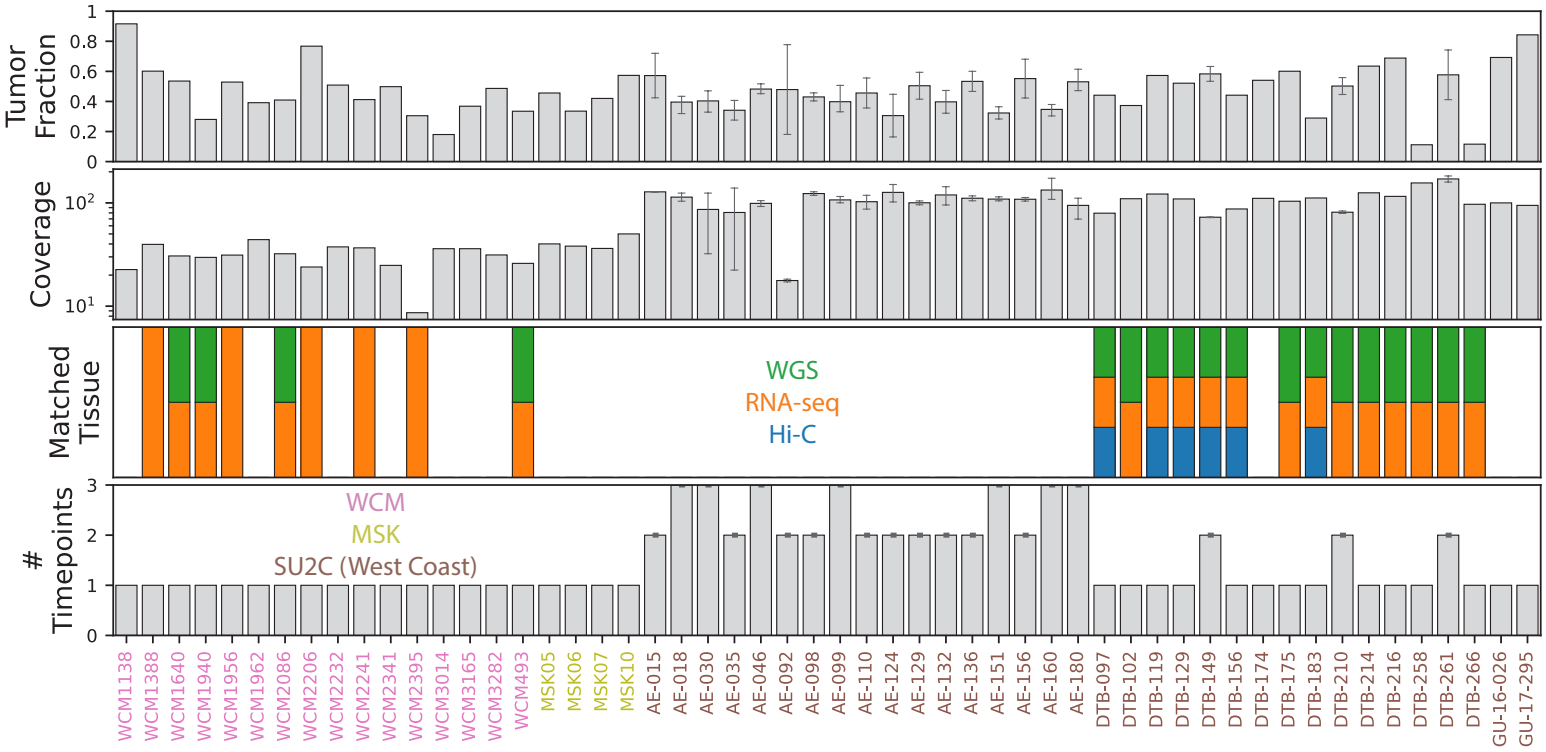

Fig. 1: Cohort overview. (A) Number of WGS cfDNA samples from plasma and WGS, RNA-seq, and Hi-C samples from tissue. Some patients have >1 sample. (B) per-sample overview of data availability for cfDNA samples.

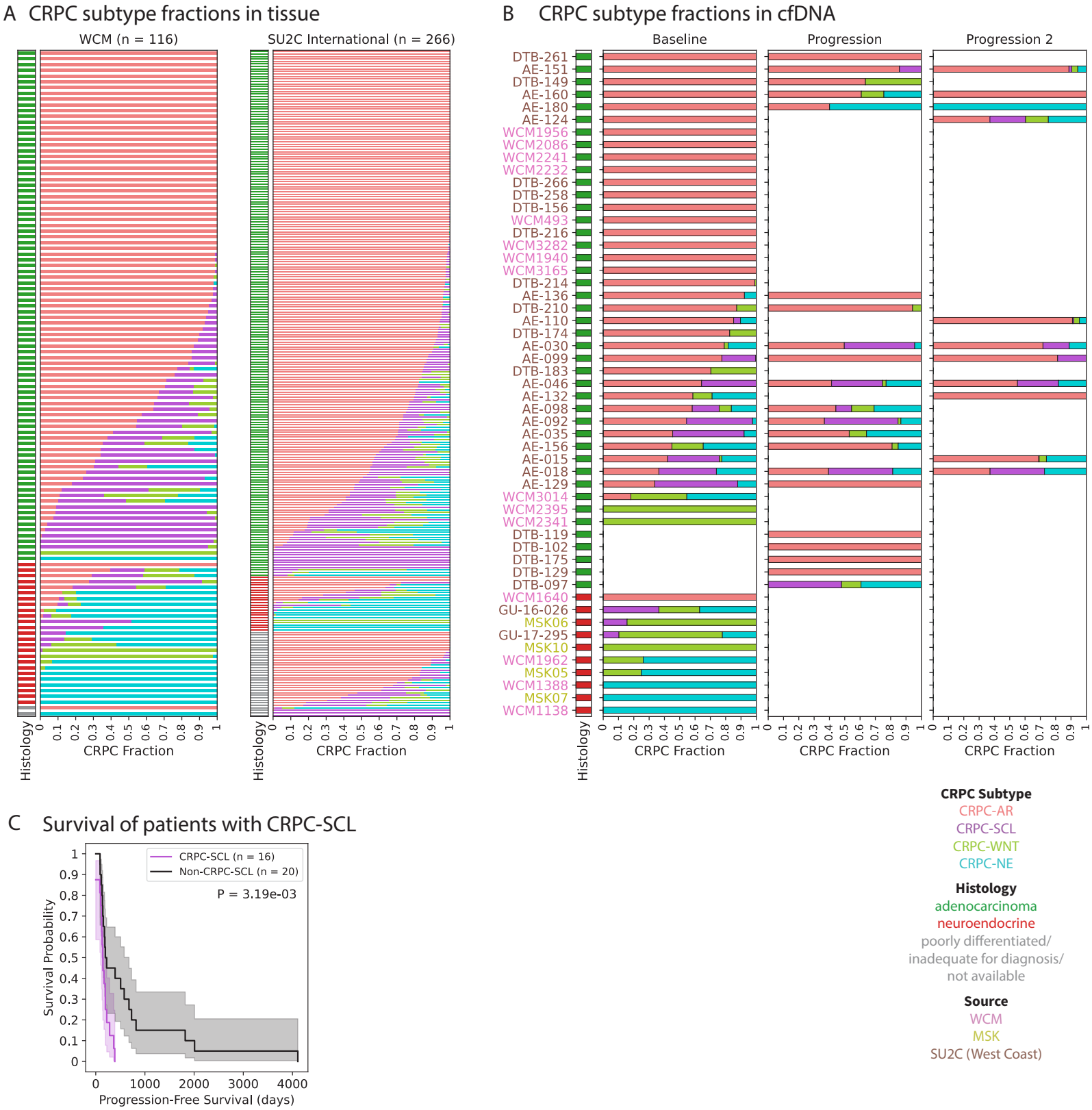

Fig. 2: CRPC subtype components in cfDNA and tissue. (A-B) CRPC fractions from deconvolution in tissue (A) and cfDNA (B) cohorts. (C) Kaplan Meier curve showing shorter progression free survival in patients with CRPC-SCL.

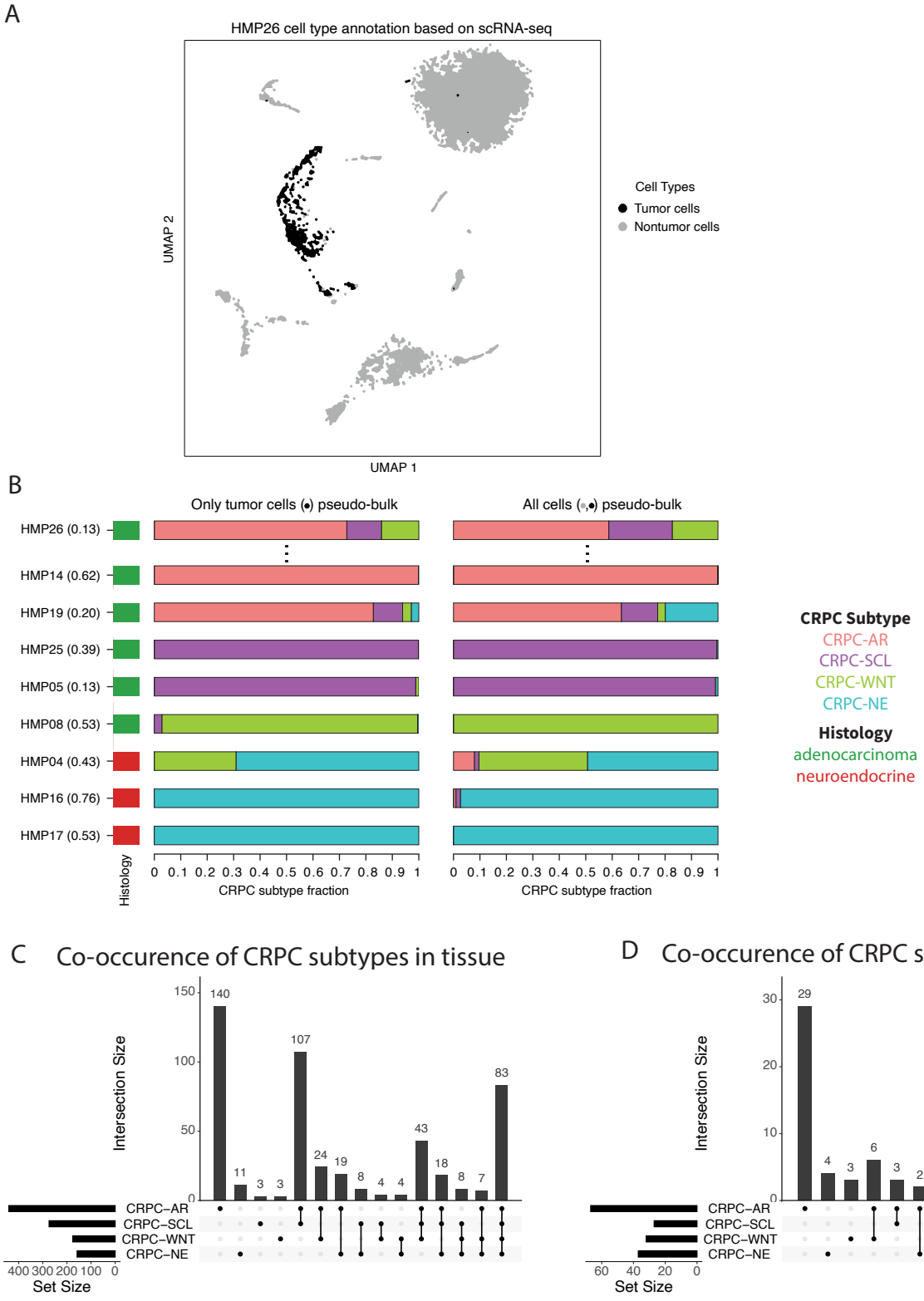

Fig. 3: Heterogeneity of CRPC subtypes. (A) Cell type annotation based on scRNA-seq in example sample. (B) CRPC fractions from deconvolution in tumor cells pseudobulk and all cells pseudobulk validates non-tumor cells do not impact subtype inference. (C-D) Upset plots showing number of samples with each CRPC subtype combination in tissue (C) and cfDNA (D). (E) ratio of number of samples with subtype mixtures to pure samples across subtypes.

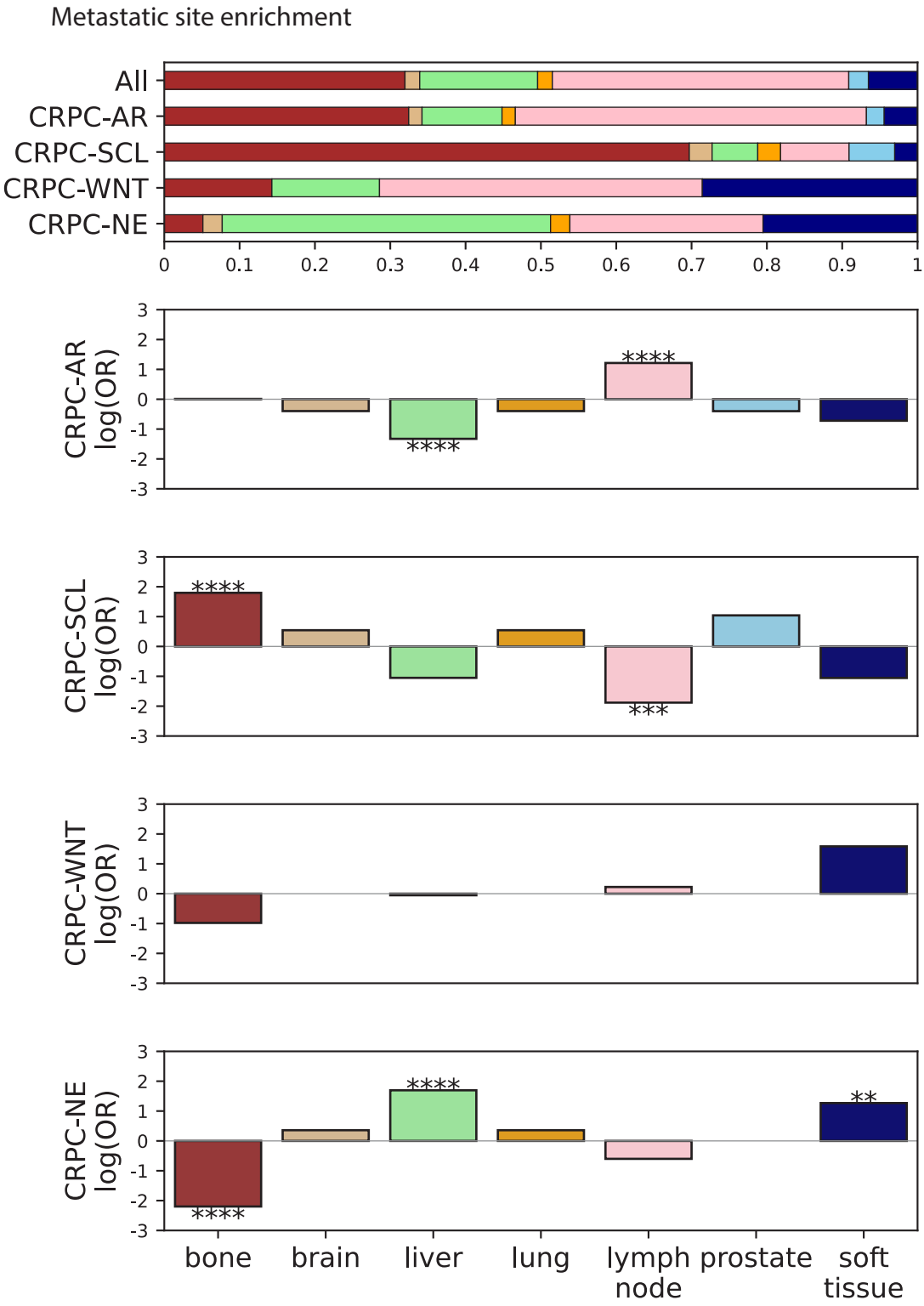

Fig. 4: Metastatic site enrichment. Fractions of samples (across all subtypes, and for within each subtype for subtype fraction ≥0.5) from each metastatic site (top), log (natural) odds ratio (OR) of a sample coming from each metastatic site across subtype fractions (bottom).

A YAP/TAZ Pathway

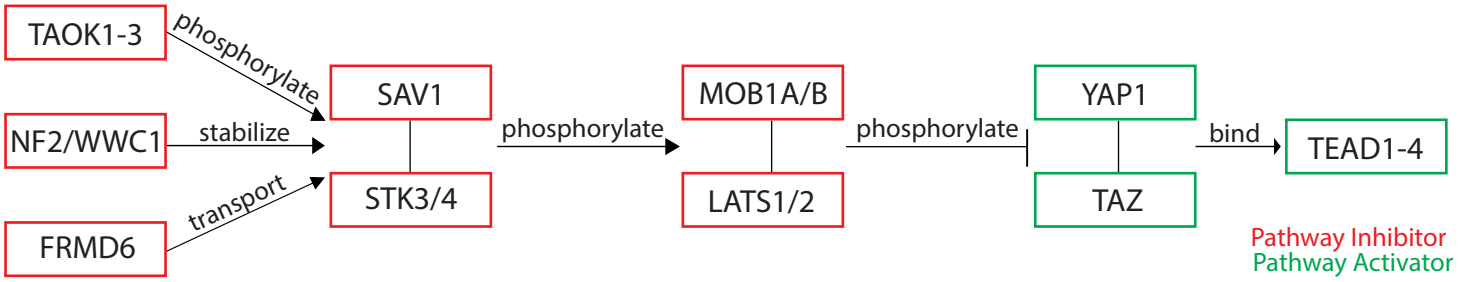

B OncoPrint

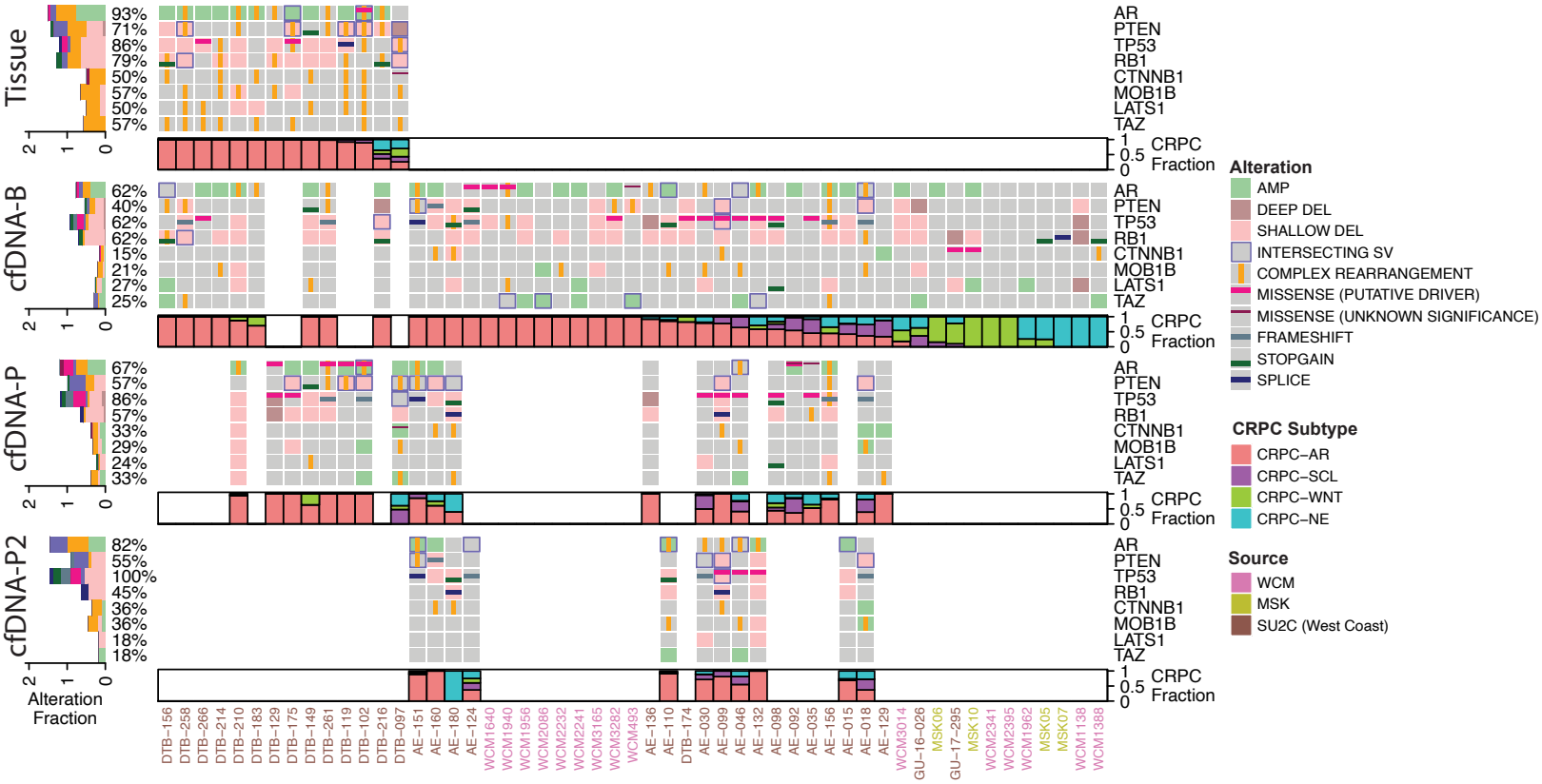

C Enrichment in CRPC-SCL

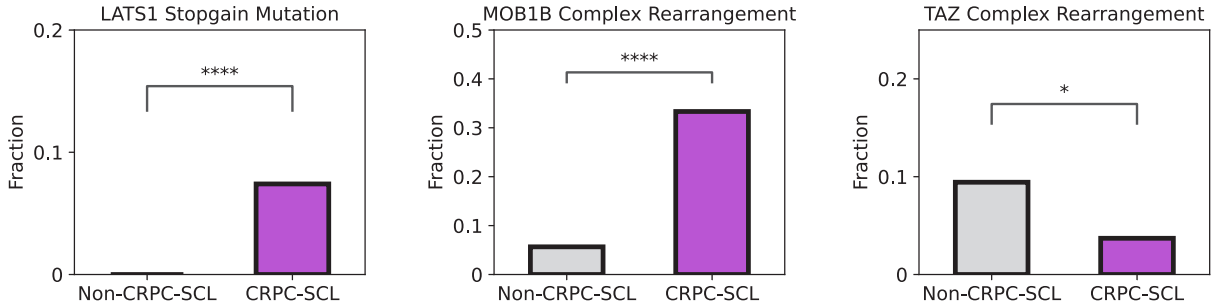

D Disappearance of CRPC-SCL upon emergence of rearrangement spanning TAZ

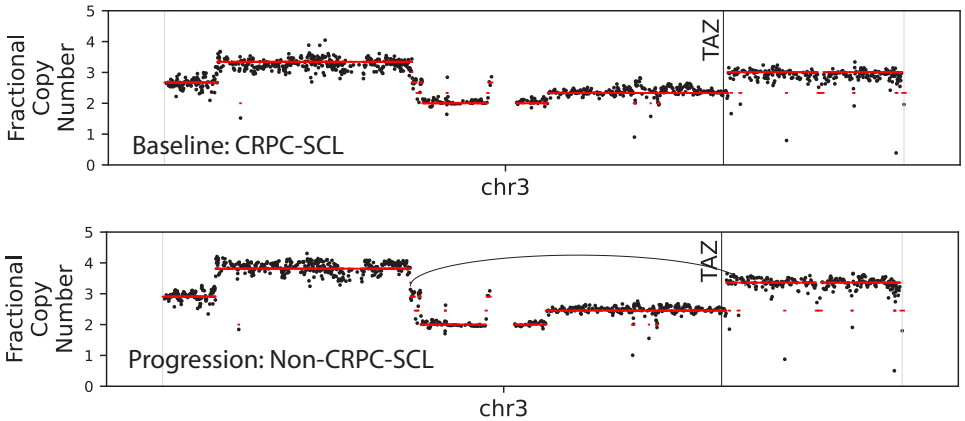

E CRPC-SCL classification ROC

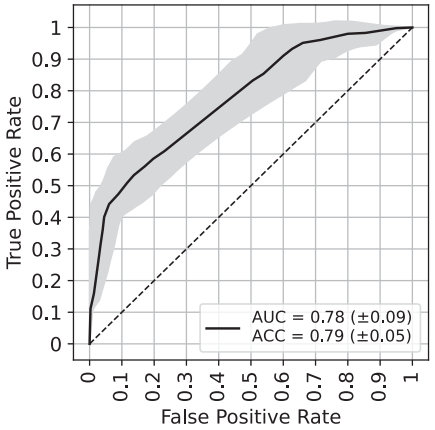

Fig. 5: YAP/TAZ pathway alterations. (A) YAP/TAZ pathway. (B) Oncoprint shows the genomic alterations for each patient in tissue and cfDNA timepoints (where available, Baseline (B), Progression (P), and Progression2 (P2)) for various genes of interest, each row is followed by the CRPC fraction of each sample from deconvolution. (C) LATS1 stopgain mutations in CRPC-SCL, complex rearrangement of chromosomes spanning MOB1B and TAZ in CRPC-SCL. (D) AE-129 signal track along chr3 across timepoints. Fractional copy number (FCN) along chr3, TAZ gene locus marked by vertical line, location of complex rearrangement shown as curved line at Progression. (E) receiver operating characteristic (ROC) curve of logistic regression model to classify samples as CRPC-SCL.

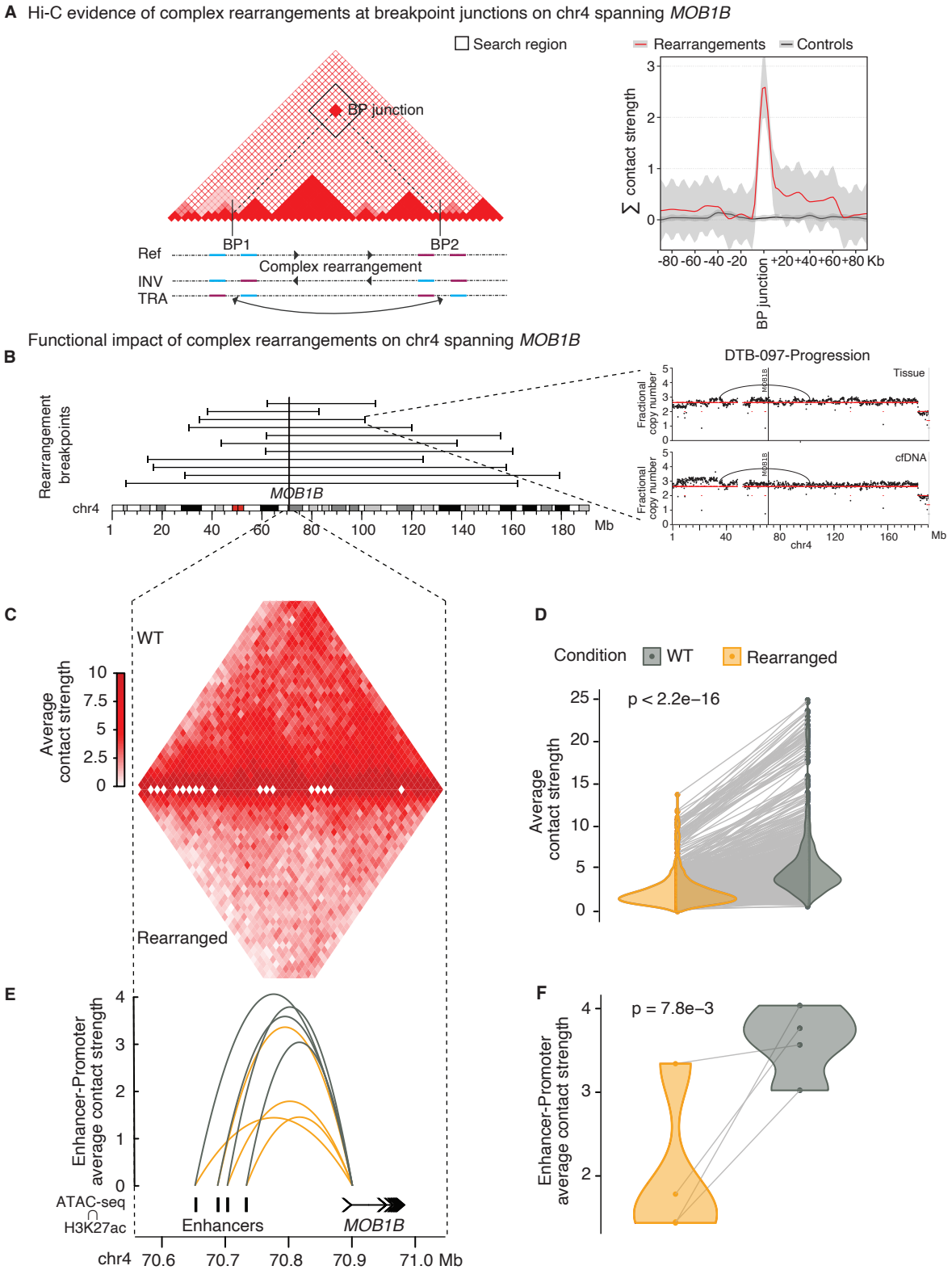

Fig. 6: Hi-C data validates structural variants and shows complex rearrangements reduce access of *MOB1B* to its regulatory elements. (A) schematic of Hi-C contact map and indices storing the connection strength of regions surrounding example inversion (INV) and translocation (TRA) breakpoints (i.e. breakpoint (BP) junction) (left) and contact strength increase in search region relative to negative control regions support evidence of rearrangement (right). (B) breakpoint locations of complex rearrangements spanning *MOB1B* in CRPC-SCL samples (left) and example of concordant breakpoints in cfDNA and matched tissue in one sample (right). (C) contact maps in TAD surrounding *MOB1B* in CRPC-SCL samples without (wildtype (WT), top) and with (rearranged, bottom) the rearrangement. (D) Strength of the contacts averaged across samples is lower in CRPC-SCL samples with the rearrangement (rearranged) compared to those without it (WT). (E) Average interaction strength between *MOB1B* promoter and its enhancers in CRPC-SCL samples with (rearranged) and without (WT) the rearrangement. (F). Strength of the enhancer-promoter interactions averaged across samples is lower in CRPC-SCL samples with the rearrangement (rearranged) compared to those without it (WT).

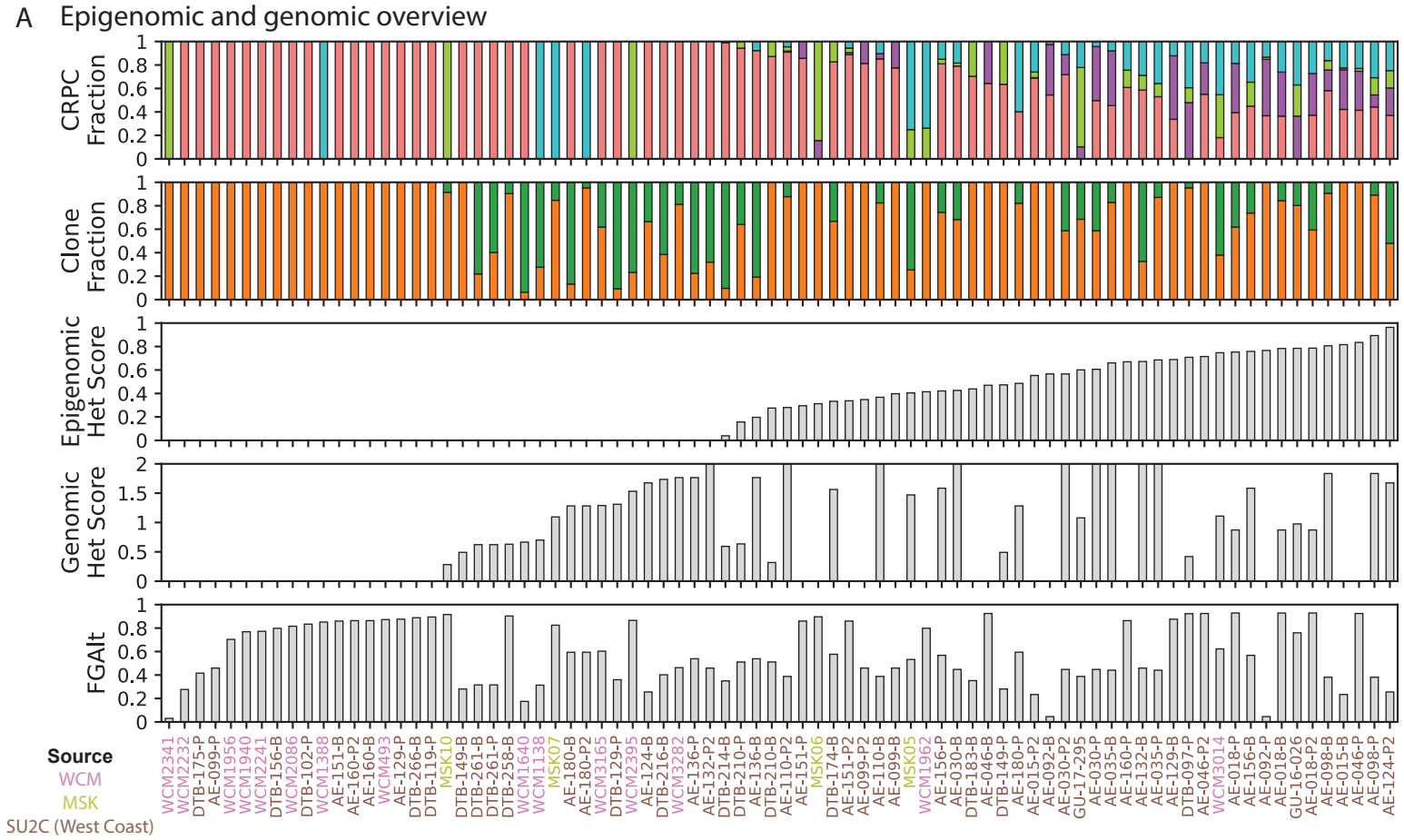

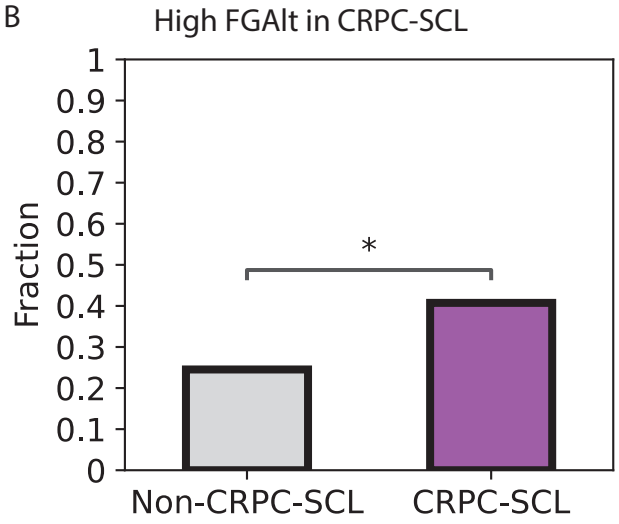

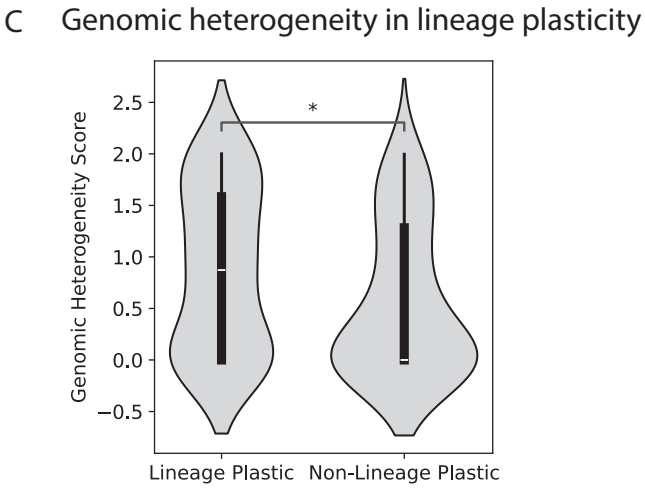

Fig. 7: Genomic heterogeneity and instability and CRPC subtypes. (A) Per-sample molecular and genomic overview: CRPC fraction from deconvolution (top row), tumor clone fraction composition (second row), molecular heterogeneity score (third row), genomic heterogeneity score (fourth row), and fraction of genome altered (last row). (B) High FGAlt enrichment in CRPC-SCL samples. (C) Genomic heterogeneity score distribution in lineage plastic and non-lineage plastic samples.